NRP1 is a receptor for mammalian orthoreovirus engaged by distinct capsid subunits

Pengcheng Shang,[1,2] Rita dos Santos Natividade,[3] Gwen M. Taylor,[1,2] Ankita Ray,[3] Olivia L. Welsh,[1,2] Kay L. Fiske,[1,2] Danica M. Sutherland,[1,2] David Alsteens,[3,4] and Terence S. Dermody[1,2,5*]

[1]Department of Pediatrics, University of Pittsburgh School of Medicine, Pittsburgh, Pennsylvania, USA

[2]Institute of Infection, Inflammation, and Immunity, UPMC Children's Hospital of Pittsburgh, Pittsburgh, Pennsylvania, USA

[3]Louvain Institute of Biomolecular Science and Technology, Université catholique de Louvain, Louvain-la-Neuve, Belgium

[4]WELBIO department, WEL Research Institute, Wavre, Belgium

[5]Department of Microbiology and Molecular Genetics, University of Pittsburgh School of Medicine, Pittsburgh, Pennsylvania, USA

*Address correspondence to Terence S. Dermody, terence.dermody@chp.edu.

SUMMARY

Neuropilins (NRPs) bind a variety of physiological ligands and serve as receptors for viruses with public health importance. However, mechanisms regulating NRP-mediated virus entry and the roles of NRPs in viral pathogenesis are not well understood. In this study, we identified murine NRP1 (mNRP1) as a mammalian orthoreovirus (reovirus) receptor. mNRP1 binds reovirus with nanomolar affinity and promotes reovirus infection. Our findings reveal a unique mechanism of virus-receptor interaction, which is coordinated by multiple interactions between distinct reovirus capsid subunits and NRP1 extracellular domains. By engineering reovirus mutants incapable of binding NRP1, we found that NRP1 contributes to reovirus dissemination and neurovirulence in mice. Collectively, our results demonstrate that NRP1 is an entry receptor for reovirus and uncover mechanisms by which NRPs promote viral entry and pathogenesis.

KEYWORDS

NRP1, reovirus, binding, infection, affinity, capsid proteins, dissemination, CNS, neuropathogenesis

37 **INTRODUCTION**

38

39 Neuropilins (NRPs) are cell-surface receptors with pleiotropic physiological functions in
40 the cardiovascular, nervous, and immune systems.[1-5] Two NRP homologs, NRP1 and
41 NRP2, bind a range of structurally diverse ligands, including vascular endothelial growth
42 factor (VEGF) isoforms and semaphorins (SEMAs).[1-5] NRPs also are used as receptors
43 or coreceptors by several pathogenic viruses,[6] including pandemic SARS-CoV-2[7-9] and
44 several herpesviruses.[10-12] Host receptors often determine viral dissemination routes
45 and tropism for discrete tissues.[13-16] The broad expression of NRPs in endothelial,
46 immune, and neuronal cells suggests roles for these receptors in viral dissemination
47 and tissue tropism. However, since NRP-null animal models are not viable,[1,2] functions
48 of NRPs in viral pathogenesis have not been confirmed.[6]

49 NRPs incorporate multiple extracellular domains with remarkable structural
50 flexibility to accommodate binding to different ligands.[3,5,17-19] NRPs engage native
51 ligands following the C-end rule (CendR), in which a conserved pocket in the
52 extracellular b1 domain binds a C-terminal polybasic R/KXXR/K motif in the ligand,[1,3]
53 which is a native C-end or produced by furin cleavage. The SARS-CoV-2-NRP1
54 interaction depends on furin cleavage of viral spike proteins and is associated with
55 membrane fusion. However, some virus-NRP interactions, including interactions
56 between human cytomegalovirus (hCMV) pentamer protein and NRP2 are independent
57 of the CendR but still appear to promote fusion.[18,19] Other herpesviruses also use NRP1
58 as a fusion protein receptor.[11,12,20] Therefore, the function of NRPs in viral entry is often
59 associated with enveloped virus fusion regardless of the CendR.

60 In this study, we identified NRP1 as an entry receptor for nonenveloped reovirus
61 and investigated functions of NRP1 in reovirus pathogenesis. Reovirus encapsidates a
62 segmented, double-stranded RNA genome in a double-layered icosahedral capsid shell
63 composed of eight capsid proteins.[21] With a robust reverse genetics system,[22] reovirus
64 is a well-established experimental system to study nonenveloped virus receptor
65 engagement, internalization, and disassembly.[23] Reovirus has a broad host range in
66 mammals[21,24] and has been linked to celiac disease in humans.[25,26] In mice, reovirus
67 establishes primary infection in the intestine and disseminates to sites of secondary
68 infection, including the CNS, by hematogenous or neural routes.[21,24] Reovirus
69 dissemination pathways and neurovirulence are extraordinarily dependent on viral
70 serotype,[24] which is likely regulated by serotype-specific neural receptors. We have
71 identified several attachment factors and receptors for reovirus and found that reovirus
72 entry involves discrete virus-receptor pairs, which influence viral pathogenesis at
73 multiple steps.[27-35] However, how reovirus receptors regulate neuropathogenesis
74 remains largely unknown.
75 In a previous genome-wide CRISPR screen for host factors that promote reovirus
76 infection, murine NRP1 (mNRP1) emerged as a top candidate[36]. Here, we validated
77 mNRP1 as a reovirus receptor and investigated the function of mNRP1 in reovirus cell
78 entry and pathogenesis. We discovered an unusual virus-receptor interaction
79 mechanism characterized by high-affinity, multi-valency, and host specificity, in which
80 distinct viral capsid subunits bind multiple NRP1 extracellular domains. Our findings
81 indicate that NRPs can function in fusion-independent entry of nonenveloped viruses
82 and demonstrate that NRP1 contributes to viral dissemination, replication in the CNS,

83 and neurovirulence in mice. This work highlights reovirus as an experimental model to
84 investigate mechanisms of NRP-mediated viral entry and its significance in viral
85 pathogenesis.
86
87 **RESULTS**
88
89 **mNRP1 promotes reovirus binding and infection**
90 In a previous whole-genome CRISPR-knockout (CRISPR-KO) screen, CRISPR-edited
91 mouse microglial BV2 cells were infected with prototype reovirus strains type 1 Lang
92 (T1L) or type 3 Dearing (T3D), and gene candidates promoting infection were identified
93 from surviving cells.[36] NRP1 was identified as the top proviral gene candidate in the
94 screen using strain T3D. We validated these results using NRP1-targeting sgRNAs to
95 eliminate expression of NRP1 in BV2 cells (**Figure S1A**) and observed that T3D
96 infection was significantly attenuated in cells lacking NRP1, while T1L infection was not
97 altered (**Figures 1A** and **S1B**).
98 CRISPR-KO screens often identify essential viral entry factors, including viral
99 receptors.[37,38] If murine NRP1 (mNRP1) serves as a reovirus receptor, overexpression
100 of mNRP1 cDNA in nonsusceptible CHO cells that lack reovirus receptors should
101 promote reovirus binding and infection.[27] Concordantly, transient mNRP1 expression
102 promoted T3D but not T1L infection, suggesting that mNRP1 functions as a receptor for
103 reovirus T3D (**Figures 1B** and **S1C**). In these experiments, human NRP1 (hNRP1) and
104 NRP2 paralogs did not promote reovirus infection.

105 To determine whether reovirus binds to mNRP1-expressing cells, we used non-
106 sialic-acid-binding (SA-) viruses (T1LSA- and T3DSA-) to eliminate attachment to
107 sialylated cell-surface proteins as a potential confounding variable[27] (**Figures 1C** and
108 **S1D**). mNRP1 overexpression promoted robust T3DSA- virus binding and modest
109 T1LSA- binding, whereas hNRP1 overexpression did not efficiently promote binding of
110 either reovirus strain. Virus binding to and infectivity of mNRP1-expressing cells was
111 blocked by preincubating cells with either mNRP1-specific antibody (**Figures 1D-E**) or
112 NRP1 ligand VEGF (**Figure 1F**) as well as preincubating reovirus with recombinant
113 mNRP1 (**Figure 1G**). These data support the specificity of mNRP1 in promoting
114 reovirus binding and infection. mNRP1 also promoted infection by another reovirus
115 strain, type 3 Abney (also called T3C87), but not the other type 3 strains tested[39]
116 (**Figure S2**), suggesting that the recognition of mNRP1 is strain-specific and not
117 serotype-specific. Collectively, ectopically expressed mNRP1 specifically promotes
118 reovirus T3D binding and infection, suggesting that mNRP1 is a reovirus receptor.
119

120 **Biophysics of reovirus-NRP1 interactions**

121 To determine whether reovirus directly binds to mNRP1, we analyzed the reovirus-
122 NRP1 interaction using a biophysical approach. In precipitation assays using
123 recombinant receptors, T3DSA- virions were efficiently bound by mNRP1 but not
124 hNRP1, while T1LSA- virions were not bound by either receptor (**Figure 2A**). To further
125 investigate the kinetics and thermodynamics of the reovirus-NRP1 binding complex,, we
126 used atomic force microscopy (AFM) to quantify virion-NRP1 interactions at the single-
127 molecule level. AFM tips covalently functionalized with T3DSA- virions were moved

128 cyclically toward and away from an mNRP1-coated surface, which allows virus-receptor
129 bonds to form and break (**Figure 2B**). Force-distance (FD) curves measuring adhesion
130 events were collected, and binding frequencies (BF) were calculated. In these
131 experiments, T3DSA- virions bound specifically to mNRP1-coated surfaces (**Figure**
132 **2C**). Virus binding was significantly reduced by preincubation with VEGF, consistent
133 with results using NRP1-expressing cells (**Figure 1F**), but preincubation with mNRP1-
134 specific mAb did not decrease binding.

135 To quantify reovirus-mNRP1 binding kinetics, the rupture force of the complex
136 was probed at different loading rates[40] (**Figures 2D** and **S3**), as previously
137 described.[27,41-43] The data were fit with the Bell-Evans model of mono-bond interactions,
138 which assumes that the energy landscape governing the bond rupture can be
139 approximated by a simple potential energy barrier [44,45] and allows the extraction of
140 kinetic parameters of molecular interactions such as the dissociation rate (k_{off}) and
141 distance to the transition state (x_u) (**Figure 2E**). For the T3DSA- reovirus-mNRP1
142 complex, the estimated k_{off} (0.15 ± 0.12 s^{-1}) and x_u (0.92 ± 0.08 nm) values indicate
143 formation of a stable complex with large conformational variability. We extracted the
144 association rate (k_{on}) by monitoring the binding frequency versus the contact time[46] (k_{on}
145 = 39.30 ± 6.85 μM^{-1} s^{-1}) and observed an equilibrium dissociation constant (K_D = 3.89 ±
146 3.69 nM) (**Figure 2E**), indicating a high-affinity interaction between T3DSA- and
147 mNRP1.

148 We also detected significant binding of T3DSA- to a recombinant hNRP1-coated
149 model surface (**Figure S4**), which was only weakly detectable in the cell-based binding
150 (**Figures 1C**) and precipitation assays (**Figure 2A**). T3DSA- binding to hNRP1 was

151 similarly fit with the Bell-Evans model and estimated to have a comparable dissociation
152 constant (K_D = 4.18 ± 2.86 nM) to that of mNRP1 but strikingly diminished k_{on},
153 suggesting different binding kinetics, which may explain the discordant binding results.
154 The physiological relevance of reovirus-NRP1 binding was further tested by
155 probing the complex on living cells expressing fluorescent-reporter mNRP1 (mNRP1$^+$)
156 (**Figure 2F**). Binding to mNRP1$^+$ cells was compared with binding to adjacent mNRP1$^-$
157 cells (**Figure 2G**). T3DSA- specifically bound mNRP1$^+$ cells (**Figures 2H-I** and **S5**).
158 Rupture-force curves derived from mNRP1$^+$ cells were overlaid on those from model
159 surfaces (**Figure 2J**; blue data points) and plotted as a histogram (**Figure 2K**). Data
160 from model surfaces and living cells were concordant, although higher-ranged rupture
161 forces representing potential multivalency were more frequent in the experiments with
162 living cells. We used the Williams-Evans model to predict forces associated with rupture
163 of simultaneous uncorrelated bonds **(Figure 2J**; red dashed line, I-VI), which showed a
164 strong match with force peaks obtained using living cells **(Figures 2J-K)**, suggesting
165 that high-ranged forces correspond with the establishment of simultaneous bonds
166 between virions and multiple receptor molecules. Such multivalent reovirus-NRP1
167 interactions may be favored on cell membranes. Overall, these biophysical data
168 demonstrate specific and high-affinity interactions between reovirus T3D and mNRP1 at
169 a single-molecule level and in a more complex live-cell system.
170

171 **Reovirus-NRP1 interactions require multiple NRP1 extracellular domains**

172 mNRP1, but not its human homolog, functions as a reovirus receptor. To define NRP1
173 domains involved in the interaction, we reciprocally exchanged the five extracellular

174 domains (a1, a2, b1, b2, and c) between murine and human homologs to construct
175 chimeric receptors[3,5] (**Figure 3A**). We reasoned that exchanging domains required for
176 reovirus binding should produce a phenotypic switch between mNRP1 and hNRP1.
177 Murine and human NRP1 homologs share substantial amino acid identity (~ 93%) in the
178 extracellular region, suggesting that reciprocal exchange of homologous domains
179 should maintain structural stability and surface expression. As anticipated, surface
180 expression of the chimeric receptors was comparable (**Figure 3B**), with the exception of
181 hNRP1 with the mNRP1 a1 domain (hNRP1-ma1). We first assessed the chimeric
182 receptors for reovirus-binding capacity (**Figure 3C**). For mNRP1 chimeras, a2 or c
183 domain exchange (mNRP1-ha2, -hc) did not diminish reovirus binding relative to WT
184 mNRP1. In contrast, b1 or b2 domain exchange (mNRP1-hb1, -hb2, -hb1b2) diminished
185 reovirus binding. For hNRP1 chimeras, substitution of the a2, b1, or b2 domain (hNRP1-
186 ma2, -mb1, -mb2, -mb1b2) increased reovirus binding relative to WT hNRP1. In
187 contrast, a1 or c domain exchange (hNRP1-ma1, -mc) did not alter binding. These
188 results suggest that multiple mNRP1 domains are required for binding reovirus.
189 We then determined the effect of NRP1 domain exchange on reovirus infectivity
190 (**Figure 3D**). For mNRP1 chimeras, infectivity was decreased when b1 or b2 were
191 exchanged (mNRP1-hb1, -hb2, -hb1b2). As expected, exchange of hNRP1 b1 or b2
192 (hNRP1-mb1, -mb2, -mb1b2) enhanced infectivity. Due to the importance of the NRP1
193 b1 domain in reovirus infection (**Figures 3C-D**), we tested the effect of CendR inhibitors
194 on reovirus infection of NRP1-expressing cells (**Figure S6**). Not surprisingly, as a
195 nonenveloped virus, reovirus infection was not diminished by treatment with small-
196 molecule inhibitors of furin and the b1 domain, suggesting that reovirus-NRP1

197 interactions do not follow the CendR. Furthermore, the mNRP1-specific mAb that blocks
198 reovirus binding to cells (**Figure 1D-E**) binds to the b1 domain (**Figure S7**). Collectively,
199 these results indicate that mNRP1 domains b1 and b2 are required for reovirus binding
200 and infection in manner independent of the CendR.

201 We also used NRP1 domain-deletion mutants as a complementary approach to
202 define domains required for reovirus binding (**Figure 3E**). Deletion of mNRP1 a1 or c,
203 which are not contained in the structurally rigid a2-b1-b2 core,[47,48] did not alter receptor
204 expression relative to WT (**Figure 3F**). Concordant with diminished reovirus binding of
205 the a1 exchange (mNRP1-ha1) (**Figure 3C**), deletion of a1 (Δa1) substantially
206 attenuated reovirus binding (**Figure 3G**) and infection (**Figure 3H**). In contrast, deletion
207 of the c domain only slightly decreased reovirus binding and did not alter infection
208 (**Figures 3G-H**). Collectively, these results indicate an essential role for the mNRP1 a1
209 domain in interactions with reovirus.

210

211 **Reovirus interactions with NRP1 require multiple capsid proteins**

212 The reovirus outer capsid is composed of heterohexamers of σ3 and μ1 proteins, in
213 which μ1 is a pedestal for σ3, and σ1 trimers embedded into λ2 pentamers at the
214 icosahedral fivefold vertices[21] (**Figure 4A**, schematic). To identify the surface-exposed
215 capsid proteins that bind mNRP1, we reciprocally exchanged gene segments encoding
216 the λ2, σ1, and σ3 proteins (L2, S1, and S4, respectively) of strains T1L and T3D using
217 reverse genetics[22] (**Figure 4A**, table). We hypothesized that exchanging essential
218 capsid protein-encoding gene segments of T3D with non-essential gene segments of
219 T1L would decrease infection of mNRP1-expressing cells and *vice versa*. For T3D

220 reassortants, L2 (λ2) exchange (T3D-T1L L2, -T1L L2+S1, and -T1L L2+S4) resulted in
221 complete loss of infectivity (**Figure 4B**), suggesting that λ2 is required for NRP1-
222 mediated reovirus infection. Conversely, S1 (σ1) or S4 (σ3) exchange (T3D-T1L S1, -
223 T1L S4, and -T1L S1+S4) did not dampen infectivity. For T1L reassortants, S1 (σ1) or
224 S4 (σ3) exchange (T1L-T3D S1, -T3D S4, and -T3D S1+S4) did not increase infectivity
225 (**Figure 4C**). In contrast, L2 (λ2) exchange (T1L-T3D L2 or -T3D L2+S1) resulted in a
226 modest infectivity increase, with L2+S4 (λ2+σ3) dual-exchange (T1L-T3D L2+S4)
227 producing the most substantial increase in infectivity. Collectively, these results suggest
228 that both λ2 and σ3 of strain T3D are required to bind NRP1, and λ2 may be more
229 important for the interaction.

230 To better understand the function of σ3 in NRP1-mediated reovirus infection, we
231 tested the interaction of mNRP1 with infectious subvirion particles (ISVPs), a reovirus
232 disassembly intermediate[21,23] (**Figures 4D-E**). ISVPs are formed by the proteolytic
233 removal of σ3 from virions during viral disassembly, while the integrity and conformation
234 of λ2 are maintained.[21,23] T3D virions and ISVPs infected cells expressing σ1 receptor
235 JAM-A, while only virions infected mNRP1-expressing cells (**Figure 4D**). Moreover,
236 recombinant mNRP1 did not capture ISVPs in precipitation assays (**Figure 4E**),
237 suggesting an essential role for σ3 in the interaction with mNRP1. Indeed, mNRP1
238 bound T3D σ3 in precipitation assays (**Figure 4F**) and did so with a ~ 25-fold higher
239 affinity than hNRP1 (K_D = 2 nM vs 49 nM), as assessed by biolayer interferometry (BLI)
240 (**Figures 4G-H**). This finding helps explain differences in reovirus infection of cells
241 expressing murine and human NRP1 homologues. Consistent with AFM results using
242 virions and model surfaces (**Figure 2C**), the σ3-NRP1 interaction was blocked by VEGF

243 (**Figure S8**). Collectively, these results indicate that outer-capsid protein σ3 of strain
244 T3D directly engages NRP1 and demonstrate an essential role of capsid turret protein
245 λ2 in strain-specific NRP1-mediated reovirus infectivity.
246

247 **Capsid turret protein λ2 contributes to NRP1 binding and is required for NRP1-**
248 **mediated reovirus infection**

249 Reovirus λ2 proteins form pentameric turrets at the virion icosahedral fivefold vertices [49-
250 51], at which λ2 and peripentameric $\mu1_3\sigma3_3$ heterohexamers may form a substructure to
251 bind NRP1 (**Figure 5A**). The λ2 turret is the viral mRNA-capping enzyme and
252 incorporates a guanylyltransferase (GTase) domain, two methyltransferase (MTase)
253 domains (2'-O-MTase and N7-MTase), and a C-terminal Flap domain[49] (**Figure 5B)**.
254 The MTase and Flap domains are partially surface-exposed (**Figures 5C** and **S9**).
255 Since λ2 is essential for reovirus infection of mNRP1-expressing cells (**Figure 4B**), it is
256 possible that polymorphic surface-exposed residues at the MTase and Flap domains
257 dictate differences in interactions with mNRP1 (**Figure 5C** and **Table S1**). We chose
258 seven and five residues in the N7-MTase and Flap domains, respectively, for further
259 analysis (**Figures 5C-D**). The five residues selected in the Flap domain are adjacent to
260 an integrin-binding motif (IBM).[35,52] Two IBMs are located within the N7-MTase and Flap
261 domains (**Figures 5B-C** and **S9**), of which the surface-exposed IBM motif (KGE) in the
262 Flap domain is required for integrin binding.[35] This motif is distal to the σ1 encapsidation
263 pore formed by assemblies of the Flap domain (**Figures 5C** and **S9**), suggesting that
264 this region of the Flap domain is sterically accessible for receptor binding and may
265 engage NRP1.

266 To test this hypothesis, we classified surface-exposed polymorphic residues
267 based on domain distribution and reciprocally exchanged polymorphic residues
268 between T1L and T3D λ2 (**Figure 5D**). Regions containing residues-of-interest in λ2
269 Flap and N7-MTase domains were annotated as region I (R I) and region II (R II),
270 respectively. We first analyzed the infectivity of mutant viruses using mNRP1-
271 expressing cells (**Figure 5E**). Substitutions in λ2 region I or II (R I or R II) of T3D
272 decreased infectivity. These results correlate well with infectivity data using T1L x T3D
273 reassortants (**Figure 4B**), as a T1L mutant virus (λ2 R I-II + σ3-T3D), engineered with
274 T3D λ2 residues in region I and II and a T3D-derived σ3-encoding S4 gene, gained the
275 capacity to infect mNRP1-expressing cells. We then analyzed effects of λ2 polymorphic
276 residue substitution on T3D-NRP1 binding (**Figures 5F-G**). Substitutions in λ2 region II
277 (λ2 R II) modestly diminished binding, whereas the combination of λ2 region I and II (λ2
278 R I-II) substitutions decreased T3D-NRP1 binding more significantly. In contrast, a T1L
279 mutant with T3D λ2 polymorphic residues and a T3D σ3 protein (λ2 R I-II + σ3-T3D)
280 gained the capacity to bind mNRP1. Additionally, infectivity (**Figure 5E**) and *in vitro*
281 binding (**Figures 5F-G**) results suggest that residues in region II of the N7-MTase
282 domain appear to contribute more substantially to the mNRP1-binding interaction than
283 residues in region I of the Flap domain. Thus, the σ1-distal region of the λ2 turret may
284 serve as an NRP1-binding interface (**Figures 5C** and **S9**). Disrupting the potential
285 binding interface on λ2 abolished infectivity but only diminished NRP1 binding,
286 suggesting that the capsid turret protein λ2 regulates an essential early step in NRP1-
287 mediated viral infection, such as internalization into the endocytic pathway.
288

289 **Sequences in outer-capsid protein σ3 required for NRP1 binding**

290 To understand how σ3 binds NRP1, we analyzed the distribution of σ3 polymorphic
291 residues in the substructure formed by λ2 and peripentameric $\mu1_3\sigma3_3$ heterohexamers
292 (**Figure 6A** and **Table S2**) and classified σ3 polymorphic residues into three patches
293 (patches [P] I, II, and III). To identify the patch that influences NRP1 binding, we
294 substituted polymorphic residues within each patch of T3D σ3 with corresponding T1L
295 residues (**Figures 6B-C**) and analyzed infectivity using NRP1-expressing cells (**Figure**
296 **6D**) and mNRP1-binding capacity (**Figure 6E**). A T3DSA- reassortant virus with a T1L
297 σ3 (σ3-T1L) was used as a loss-of-function control. Substitutions in both patch I and III
298 (σ3 P I-III) significantly decreased infectivity (**Figure 6D**), which was reduced to a level
299 comparable to that of the T1L S4 reassortant (σ3-T1L). Since polymorphic residue
300 substitutions in λ2 only partially disrupted mNRP1 binding (**Figures 5F-G**), we
301 introduced λ2 residue substitutions (R I-II) into the T3D σ3 mutant viruses to construct a
302 virus that should be incapable of binding mNRP1 (mNRP1-blind) (**Figure 6C**) and
303 tested the effect on mNRP1-binding capacity (**Figures 6E** and **S10A**). Infectivity results
304 were largely concordant with binding results. No obvious effect was observed by
305 substitutions in σ3 patch II, whereas polymorphic residues in σ3 patch I, which is most
306 proximal to the putative binding interface in λ2, modestly altered NRP1 binding. In
307 contrast, polymorphic residues in σ3 patch III contribute more substantially to mNRP1
308 binding, as incorporation of substitutions in λ2 (σ3 P I-III + λ2 R I-II) further reduced
309 mNRP1-binding capacity to the level of background (**Figures 6E** and **S10A**). Therefore,
310 this T3DSA- mutant (σ3 P I-III + λ2 R I-II) was considered to be mNRP1-blind.
311 Reciprocal exchange of the polymorphic residues in σ3 patch III alone between T1L and

312 T3D (**Figure 6F**) further confirmed the importance of patch III for NRP1-mediated
313 infectivity (**Figure 6G**) and mNRP1-binding capacity (**Figures 6H** and **S10B**). These
314 results indicate that interactions with mNRP1 are regulated by polymorphic residues in
315 outer-capsid protein σ3, which may belong to distinct σ3 protomers in the $\mu1_3\sigma3_3$
316 heterohexamer (**Figure 6A**).
317
318 **NRP1 contributes to reovirus dissemination and neurovirulence in mice**
319 Neurotropic reovirus disseminates using hematogenous and neural routes to infect
320 neurons in the CNS and cause lethal encephalitis.[24] Expression of NRP1 by vascular,
321 immune, and nervous system cells suggests that this receptor contributes to reovirus
322 dissemination and neuropathogenesis. We first tested T3D infection of primary cortical
323 neurons and observed decreased infectivity following preincubation of cells with
324 mNRP1-specific mAb (**Figures 7A** and **S11A**). We then tested infectivity of neurons by
325 NRP1-binding mutants (NBMs) including the loss-of-function λ2 mutant (R I-II) and the
326 dual σ3 and λ2 mutant (P I-III + R I-II) (**Figures 7C-D**), which were re-named NBM1 and
327 NBM2 for convenience. NBM1 has attenuated NRP1-binding capacity and does not
328 infect NRP1-expressing cells (**Figures 5E-G**), while NBM2 is NRP1-blind (**Figure 6E**).
329 As an important control, NBM1 and NBM2 are capable of infecting JAM-A-expressing
330 L929 cells and produce titers comparable to those of WT virus (**Figure 7B**). Concordant
331 with the antibody-blockade effects, NBMs showed reduced infectivity (**Figures 7C** and
332 **S11B**) and replication (**Figure 7D**) following inoculation of primary neurons, which
333 suggests a potential function for NRP1 in reovirus replication in the nervous system.

334 Since embryonic development requires NRP1,[1,2] we compared replication
335 capacity and virulence of WT and NBM viruses to determine whether NRP1 functions in
336 reovirus pathogenesis (**Figures 7E-G**). We first analyzed viral replication and virulence
337 following intracranial inoculation (**Figures 7E-F**), which circumvents dissemination
338 routes and allows establishment of infection directly in the CNS. Viral titers in the brain
339 of NBM-inoculated mice were significantly lower than those of WT virus (**Figure 7E**).
340 Mice inoculated with NBM viruses also had improved survival relative to those
341 inoculated with WT virus (**Figure 7F**). These results suggest that NRP1 is required for
342 maximal reovirus replication and full neurovirulence in mice. We tested whether NRP1
343 expression influences reovirus neurotropism by analyzing the distribution of viral antigen
344 in the brain of inoculated mice (**Figure S12**). In these experiments, NBM and WT
345 viruses infected similar brain regions in samples with comparable viral loads, suggesting
346 that NRP1 does not influence reovirus neurotropism.
347 Systemic pathogen infection requires (i) traverse of physiological barriers
348 separating blood and tissue[53,54] or (ii) transit through nerves innervating peripheral
349 tissues to reach distant sites.[53,54] To investigate whether NRP1 contributes to reovirus
350 hematogenous or neural dissemination, we inoculated mice intramuscularly with WT or
351 NBM viruses (**Figure 7G**). Intramuscular inoculation was used in these experiments due
352 to the relative instability of strain T3D in the proteolytically active intestinal lumen.[55,56]
353 Tissues were harvested at early (2 days post-inoculation [DPI]), medium (4 DPI), and
354 late (8 DPI) stages of infection. Viral titers in the blood (viremia) of NBM-inoculated mice
355 were significantly lower than those of WT virus, suggesting that NRP1 contributes to
356 hematogenous dissemination (**Figure 7G**). In addition, viral titers in the spinal cord and

357 brain of NBM-inoculated mice were significantly lower than those of WT virus at 2 and 4
358 DPI, which provides further evidence of a function for NRP1 in viral dissemination from
359 muscle to the CNS. Following intramuscular inoculation, virus in the spinal cord at early
360 and medium timepoints is mainly attributable to neural dissemination.[53] Therefore, it is
361 possible that NRP1 also contributes to neural dissemination, consistent with a function
362 for NRP1 in reovirus infection of neurons (**Figure 7A** and **7C-D**).
363 NBM2, which is incapable of binding NRP1, had the most attenuated phenotypes
364 in replication and virulence in mice (**Figures 7E-G**), while NBM1 had more intermediate
365 phenotypes. The correlation between NRP1-binding capacity and pathogenicity further
366 underscores the importance of NRP1 in reovirus pathogenesis. Collectively, these data
367 demonstrate that NRP1 contributes to reovirus dissemination, replication in the CNS,
368 and neurovirulence.
369
370 **DISCUSSION**
371
372 In this study, we identified NRP1 as a reovirus receptor and present biophysical and
373 functional characterization of reovirus-NRP1 interactions. Our work establishes reovirus
374 as a nonenveloped virus that uses NRP1 as a receptor and uncovers an unusual virus-
375 receptor interaction mechanism, in which reovirus-NRP1 binding appears to be a step-
376 wise process orchestrated by multiple interactions between distinct viral capsid subunits
377 and NRP1 domains. Investigation of the biophysical dynamics of NRP1-mediated
378 reovirus infection expands an understanding of multi-faceted ligand-NRP interactions
379 and will contribute to studies of ligand-induced NRP endocytosis and signaling. We

380 further discovered that NRP1 is a receptor for reovirus dissemination and
381 neurovirulence, providing experimental support for a function of NRPs in viral
382 pathogenesis.[6] Collectively, our studies establish reovirus as a model to investigate
383 mechanisms by which viruses use NRPs as entry receptors.

384 Viruses interact with NRPs using different mechanisms and do not always follow
385 the canonical CendR. The SARS-CoV-2-NRP1 interaction is CendR-dependent,[7-9] as
386 furin cleavage at the spike protein S1-S2 junction exposes the S1 C-end motif to bind
387 the NRP1 b1 domain and primes S2 for membrane fusion. Some enveloped viruses
388 with furin-activated fusion machinery have converged on similar requirements for NRPs
389 as co-receptors.[6] However, binding of hCMV to NRP2 is CendR-independent.[18,19] The
390 NRP2 a2, b2, and possibly a1 domains bind the hCMV pentamer. Even though the b1
391 domain is not engaged, pentamer-NRP2 binding may achieve an effect comparable to
392 furin-activated fusion, which possibly uncouples the pentamer from the gB protein and
393 subsequently activates gB to initiate the fusion process. NRP1 also serves as a receptor
394 for gB of other herpesviruses,[11,12,20] indicating that NRP binding is associated with
395 fusion during enveloped virus entry independent of CendR use. Here, we demonstrate
396 that NRPs also can serve as receptors for nonenveloped viruses. Reovirus-NRP1
397 binding requires the NRP1 a1, b1, and b2 domains (**Figure 3**), and the engagement of
398 the b1 domain does not require the CendR (**Figure S7**), which differs from the SARS-
399 CoV-2-NRP1 interaction. Moreover, a1-b1-b2 engagement differs from another CendR-
400 regulated multiple-domain binding mode, exemplified by the NRP1-plexinA4-sema3a
401 complex,[17] which additionally involves a1 and a2 domains. Therefore, the reovirus-
402 NRP1 binding mechanism further diversifies ligand-NRP interaction strategies. Our

403 study also shows that NRP1 binding can mediate fusion-independent entry of
404 nonenveloped viruses, which expands the utility of NRPs as viral entry receptors.
405 We propose a step-wise model of reovirus-NRP1 interactions (**Figure S13**) in
406 which the unbound NRP1 extracellular region adopts an "upright" conformation (**i**)
407 containing a structurally rigid a2-b1-b2 core as well as a1 and c domains with a more
408 flexible orientation.[17,47] In the initial contact, we think reovirus σ3 patch III residues bind
409 the NRP1 a1 domain (**ii**), subsequently triggering a conformational change in NRP1 to
410 expose the b1-b2 domains to bind both σ3 and λ2 (**iii**). The broad contact interface
411 ensures a strong and stable interaction to trigger ligand uptake. Long and disordered
412 linkers in the NRP1 extracellular region[17] ensure conformational flexibility. Unlike SARS-
413 CoV-2 and hCMV, which bind NRP with protruding envelope proteins,[7-9] the reovirus-
414 NRP1 interaction requires minimally-protruding outer-capsid protein σ3 and pedestal
415 protein λ2. Our reovirus-NRP1 interaction model explains functions of the NRP1 a1, b1,
416 and b2 domains and the engagement of structurally distinct capsid subunits and
417 provides guidance for future structural analysis, which will confirm the direct contact
418 between λ2 protein with NRP1 domains and elucidate the reovirus-NRP1 binding
419 kinetics.
420 Broad NRP tissue expression raises the possibility that these receptors function
421 in viral dissemination and tissue tropism.[1,2,4] Previous studies provide some information
422 about the roles of NRPs in viral infection of specific cell types.[6] For example, NRP1 may
423 influence susceptibility of nasopharyngeal epithelial cells to Epstein-Barr virus
424 infection,[11] mesenchymal stem cells to Kaposi's sarcoma-associated herpesvirus
425 infection,[12] and astrocytes and neurons to SARS-CoV-2 infection.[57,58] NRP2 may be

426 used as a receptor for hCMV infection of epithelial and endothelial cells.[10] However, the
427 roles of NRPs in viral pathogenesis remain largely unknown. Reovirus is a genetically
428 tractable model to study virus-host interactions. Diversity in receptor use and
429 pathological phenotype can be ascribed to specific viral gene segments,[27,28,43,59] which
430 enabled determination of the reovirus proteins required for NRP1 binding (**Figures 4A-**
431 **C**). Furthermore, high-resolution structures of reovirus capsid proteins[49-51,60,61] allowed
432 for molecular modeling and engineering of viral mutants incapable of binding NRP1
433 (**Figures 5-6**). These mutants were instrumental in elucidating functions of NRP1 in viral
434 pathogenesis (**Figure 7**). Our findings indicate that NRP1 is required for efficient
435 reovirus dissemination and full neurovirulence, which may be functions of NRP1 shared
436 by other neurotropic viruses.

437 Neurotropic reovirus disseminates using hematogenous and neural routes. Our
438 finding that NRP1 contributes to reovirus dissemination raises several important
439 questions. For hematogenous dissemination, it is unclear (i) whether NRP1 facilitates
440 viral entry at the basolateral surface of endothelial cells for release of viral progeny from
441 the apical surface,[54] similar to the function of JAM-A in reovirus dissemination,[62,63] and
442 (ii) whether NRP1 allows virus to bind or invade leukocytes for bloodstream
443 dissemination.[54] For neuronal dissemination, it is not known whether the distribution of
444 NRP1 in neurons (cell body, dendrite, axon, or synapse) regulates interneuronal
445 transmission.[64] Use of *in vitro* models of physiological barriers[54] and synapses[65] should
446 allow genetic ablation of NRP1 expression to define how NRP1 regulates viral
447 dissemination.

448 Reovirus σ1 fibers bind endothelial receptor-JAM-A for hematogenous
449 dissemination[30] and unidentified serotype-specific neural receptors for neurotropism.[59]
450 However, reovirus capsid proteins other than σ1 bind receptors that maximize the
451 efficiency of reovirus infection of neurons and contribute to neurovirulence. The reovirus
452 σ3 protein binds to human NgR1,[43] murine PirB,[27] and murine NRP1 (this study), which
453 are required for efficient neuronal infection. From infection studies using mice, we
454 hypothesize that PirB and NRP1 function to accelerate the establishment of infection in
455 the CNS. Following intracranial inoculation or dissemination from peripheral sites,
456 physiological barriers and antiviral immune responses may constrain reovirus infection
457 in the CNS and subsequent interneuronal spread. PirB and NRP1 may allow reovirus to
458 overcome these bottlenecks, perhaps by enhancing viral entry into neurons or
459 transmission across synapses. Our hypothesis is supported by the functions of non-σ1
460 receptors in reovirus replication and pathology in the CNS[27] (**Figures 7E-F**). In the case
461 of NRP1, NBMs replicate less efficiently in the murine brain at early times following
462 inoculation but eventually reach titers comparable to WT virus in some mice at later
463 times. Mice inoculated with either WT or NBM viruses show neuropathological signs at
464 8-13 DPI. However, the enhanced survival of NBM-inoculated mice relative to those
465 inoculated with WT virus suggests that NBM viruses overcome replication bottlenecks
466 inefficiently, as shown by mice with low viral loads in the brain at 8 DPI. Therefore, we
467 conclude that non-σ1 receptors maximize reovirus replication and neurovirulence.
468 The reovirus σ1 trimer has the potential to extend ~ 400 Å from the virion
469 surface,[66] which may sterically hinder λ2 binding to the ~ 160 Å NRP1 ectodomain.[67]
470 This hypothetical constraint may be alleviated by the relatively low σ1 encapsidation

471 efficiency of strain T3D relative to strain T1L,[68] which may increase access to the non-
472 protruding capsid proteins required for NRP1 binding. This hypothesis is supported by
473 our observation that gain-of-function mutations in T1L failed to increase NRP1-binding
474 capacity and infectivity to that of T3D (**Figures 5E-G** and **6G-H**). Moreover, the potential
475 functional redundancy of NRP1 and σ1 receptors in endothelial and neuronal cells may
476 allow NRP1 to be a receptor for certain neurotropic reovirus strains with low σ1
477 encapsidation efficiency.[69] This hypothetical trade-off of σ1 encapsidation efficiency and
478 NRP1 binding rationalizes the engagement of NRP1 as a co-receptor for viral entry and
479 provides an evolutionary explanation for its function in pathogenesis.

480 Mammalian orthoreovirus is a generalist pathogen with a broad mammalian host
481 range including humans. Acquisition of the capacity to bind a conserved receptor like
482 NRP1 may lower cross-species transmission barriers. Pathological outcomes of viral
483 infection often exert selective pressure on host receptors.[70] NRP1 is the third identified
484 host-specific receptor for reovirus,[27-29] suggesting that reovirus influences the
485 evolutionary trajectory of receptor proteins. Reovirus also may balance host-to-host
486 transmission and virulence by using different entry receptors during co-evolution with
487 different host species. Structure-guided evolutionary analysis of reovirus-receptor
488 interactions will help define viral and host factors governing genetic resistance or
489 susceptibility to reovirus infection in mammals, facilitate assessment of the epidemic
490 potential of reovirus variants, and foster countermeasure development.

ACKNOWLEDGEMENTS

We are grateful to members of the Alsteens, Dermody, and Prasad laboratories for many useful discussions. We thank the UPMC Children's Hospital of Pittsburgh Flow Cytometry Core for flow cytometry assistance. We thank Dr. Neetu Neetu and Dr. B. V. Venkataram Prasad from Baylor College of Medicine for assisting protein docking simulations.

This work was supported by U.S. Public Health Service award R01 AI174526 (P.S., O.L.W., D.M.S., and T.S.D.), UPMC Children's Hospital of Pittsburgh (P.S.), and the Heinz Endowments (T.S.D.). Additional support was provided by the Université catholique de Louvain, the Fonds National de la Recherche Scientifique (F.R.S.-FNRS), the European Union (ERC, SingViroPhys, Project 101088316), and the FNRS-Welbio (grant number CR-2019S-01). D.A. is a Senior Research Associate of the FNRS. The funders had no role in study design, data collection and analysis, decision to publish, or preparation of the manuscript.

AUTHOR CONTRIBUTIONS

P.S. conceived, designed, and conducted experiments, analyzed data, contributed materials and analytic tools, and drafted the paper. R.D.S.N., A.R., and D.A. conceived and designed experiments, contributed materials and analytic tools, and analyzed data. G.M.T., O.L.W., K.F., and D.M.S. conceived, designed, and conducted experiments.

T.S.D. conceived and designed experiments, analyzed data, and drafted the paper. All authors reviewed, critiqued, and provided comments on the manuscript.

DECLARATION OF INTERESTS

The authors declare no competing interests.

519 **STAR METHODS**

520 **KEY RESOURCES TABLE**

REAGENT or RESOURCE	SOURCE	IDENTIFIER
Cells		
Murine L929 fibroblast cells	Lab preservation	N/A[a]
Chinese hamster ovary (CHO) cells	Lab preservation	N/A
Murine microglial BV2 cells	Lab preservation	N/A
Baby hamster kidney (BHK) cells stably expressing T7 polymerase (BHK-T7)	Lab preservation	N/A
Primary murine cortical neurons	Current study	N/A
Antibodies		
Rat anti-mouse NRP1 mAb	Biolegend	Cat #145202
Mouse anti-human NRP1 mAb	Biolegend	Cat #354502
Rat PE anti-mouse NRP1 mAb	Biolegend	Cat #145204
PE Rat IgG2a, κ isotype control	Biolegend	Cat #400508
Mouse APC anti-human NRP1 mAb	Biolegend	Cat #354505
Purified rat IgG2a, κ isotype control	Biolegend	Cat #400502
Purified mouse IgG2a, κ isotype control	Biolegend	Cat #400202
Goat anti-rat IgG (H+L) cross-adsorbed secondary antibody, Alexa Fluor™ 488	Thermo Fisher	Cat #A-11006
Goat anti-mouse IgG (H+L) highly cross-adsorbed secondary antibody, Alexa Fluor™ 488	Thermo Fisher	Cat #A-11029
Goat anti-rabbit IgG (H+L) highly cross-adsorbed secondary antibody, Alexa Fluor™ 488	Thermo Fisher	Cat #A-11034
Rabbit anti-mouse NRP1 mAb	Cell Signaling	Cat #3725S
Rabbit anti-myc tag mAb	Cell Signaling	Cat #2278S
Rabbit anti-reovirus polyclonal antibody	Lab preservation	N/A
Plasmids		
lentiCRISPRv2-blast	Addgene	Cat #52963
lentiCRISPRv2-blast-mNRP1 sgRNA1	Current study	N/A
lentiCRISPRv2-blast-mNRP1 sgRNA2	Current study	N/A
pCDNA3.1	Lab preservation	N/A

pCDNA3.1-hJAM-A	Lab preservation	N/A
pCDNA3.1-hCAR	Lab preservation	N/A
pYX-Asc-mNRP1	Dharmacon	Cat #MMM1013-202859215
MAC-tag-c-hNrp1	Addgene	Cat #158384
pCMV3-mNRP2	Sino Biological	Cat #MG57465-UT
pCR-Topo-hNRP2	Dharmacon	Cat #MHS6278-211687836
pCDNA3.1-mNRP1	Current study	N/A
pCDNA3.1-hNRP1	Current study	N/A
pCDNA3.1-hNRP2	Current study	N/A
pCDNA3.1-mNRP1-ha1	Current study	N/A
pCDNA3.1-mNRP1-ha2	Current study	N/A
pCDNA3.1-mNRP1-hb1	Current study	N/A
pCDNA3.1-mNRP1-hb2	Current study	N/A
pCDNA3.1-mNRP1-hb1b2	Current study	N/A
pCDNA3.1-mNRP1-hc	Current study	N/A
pCDNA3.1-hNRP1-ma1	Current study	N/A
pCDNA3.1-hNRP1-ma2	Current study	N/A
pCDNA3.1-hNRP1-mb1	Current study	N/A
pCDNA3.1-hNRP1-mb2	Current study	N/A
pCDNA3.1-hNRP1-mb1b2	Current study	N/A
pCDNA3.1-hNRP1-mc	Current study	N/A
pCDNA3.1-mNRP1-Δa1	Current study	N/A
pCDNA3.1-mNRP1-Δc	Current study	N/A
pcDNA3.1(+)IRES GFP	Addgene	Cat #51406
pcDNA3.1(+)-mNRP1-IRES-GFP	Current study	N/A
T3D and T1L reverse genetic system	Previous study[22]	N/A
pT7-T3D L2 Flap (R I)	Current study	N/A
pT7-T3D L2 N7MTase (R II)	Current study	N/A
pT7-T3D L2 Flap+N7MTase (region I-II)	Current study	N/A
pT7-T3D S1 R202W (SA-blind mutant)	Current study	N/A
pT7-T1L S1 S370P/Q371E (SA-blind)	Previous study[59]	N/A
pT7-T1L L2 Flap+N7MTase (R I-II)	Current study	N/A
pT7-T3D S4 patch I (σ3 P I)	Current study	N/A
pT7-T3D S4 patch I-II (σ3 P I-II)	Current study	N/A
pT7-T3D S4 patch I-III (σ3 P I-III)	Current study	N/A
pT7-T3D S4 patch III (σ3 P III)	Current study	N/A
pT7-T1L S4 patch III (σ3 P III)	Current study	N/A

Recombinant reoviruses		
WT T3D	Lab preservation	N/A
WT T1L	Lab preservation	N/A
T3DSA- (σ1 R202W/T249I (R202W: SA-blind; T249I: protease-resistant) (only used in cell-based binding assays, ISVP preparation, and AFM assays)	Lab preservation	N/A
T3DSA- (σ1 R202W)	Current study	N/A
T1LSA- (σ1 S370P/Q371E)	Previous study[59]	N/A
T3D-T1L L2	Current study	N/A
T3D-T1L S1	Current study	N/A
T3D-T1L S4	Current study	N/A
T3D-T1L L2+S1	Current study	N/A
T3D-T1L S1+S4 (also called T3D-RV)	Previous study[25]	N/A
T3D-T1L L2+S4	Current study	N/A
T1L-T3D L2	Current study	N/A
T1L-T3D S1	Current study	N/A
T1L-T3D S4	Current study	N/A
T1L-T3D L2+S1	Current study	N/A
T1L-T3D S1+S4	Current study	N/A
T1L-T3D L2+S4	Current study	N/A
T3D λ2 Flap (λ2 R I)	Current study	N/A
T3D λ2 N7MTase (λ2 R II)	Current study	N/A
T3D λ2 Flap+N7MTase (λ2 R I-II)	Current study	N/A
T3DSA- λ2 Flap (λ2 R I)	Current study	N/A
T3DSA- λ2 N7MTase (λ2 R II)	Current study	N/A
T3DSA- λ2 Flap+N7MTase (λ2 R I-II)	Current study	N/A
T1LSA- λ2 Flap+N7MTase + T3D σ3 (λ2 RI-II + σ3-T3D)	Current study	N/A
T3DSA- σ3 patch I	Current study	N/A
T3DSA- σ3 patch I-II	Current study	N/A
T3DSA- σ3 patch I-III	Current study	N/A
T3DSA- σ3 patch I + λ2 Flap+N7MTase (σ3 P I + λ2 R I-II)	Current study	N/A
T3DSA- σ3 patch I-II + λ2 Flap+N7MTase (σ3 P I-II + λ2 R I-II)	Current study	N/A
T3DSA- σ3 patch I-III + λ2 Flap+N7MTase (σ3 P I-III + λ2 R I-II)	Current study	N/A

T3DSA- σ3 patch III	Current study	N/A
T3DSA- σ3 patch III + λ2 Flap+N7MTase (σ3 P III + λ2 R I-II)	Current study	N/A
T1LSA- σ3 patch III	Current study	N/A
T1LSA- σ3 patch III + λ2 Flap+N7MTase (σ3 P III + λ2 R I-II)	Current study	N/A
Recombinant proteins		
mNRP1-Fc	Sino Biological	Cat #50509-M38H
hNRP1-Fc	R&D Systems	Cat #10455-N1-050
mNRP1-His	Sino Biological	Cat #50509-M08H-50
hNRP1-His	Acro Biosystems	Cat #15817367
Murine VEGF164	Acro Biosystems	Cat #VE4-M4216
Human VEGF165	Acro Biosystems	Cat #16408149
T3D σ3 (*E.coli* expression, precipitation assays)	Cosmo Bio	Cat #CSB-EP365971RCHa0-20
T3D σ3 (Insect cell expression, BLI assay)	Gentaur	Cat #GEN1097713
Chemicals and kits		
Alexa Fluor™ 647 NHS ester	Thermo Fisher	Cat #A37573
Sodium bicarbonate	Fisher Scientific	Cat #BP328-500
Furin inhibitor I (Decanoyl-RVKR-CMK)	Sigma-Aldrich	Cat #344930
Furin inhibitor II (Hexa-D-arginine amide)	Sigma-Aldrich	Cat #SCP0148
EG 00229 (trifluoroacetate salt)	Cayman Chemical	Cat #33937
Dimethyl sulfoxide	Sigma-Aldrich	Cat #D2650
Invitrogen™ Colloidal Blue Staining Kit	Thermo Fisher	Cat #LC6025
Pierce™ Protein G Magnetic Beads	Thermo Fisher	Cat #88848
2x Laemmli loading buffer	Bio-Rad	Cat #1610737
4x Laemmli Sample Buffer	Bio-Rad	Cat #1610747
Xylenes, histological grade	Sigma-Aldrich	Cat #534056
Absolute ethanol, molecular biology grade	Fisher Scientific	Cat #200GMP0125
NucleoBond® Xtra Midi EF	Takara Bio	Cat #740420.50
Polysciences Aqua-Poly/Mount	Polysciences	Cat #18606
Chloroform	Sigma-Aldrich	Cat #288306-100ML
APTES	Sigma-Aldrich	Cat #A3648-100ML
Ald-Ph-PEG24-NHS ester	Broadpharm	Cat # BP-24093
Triethylamine	Sigma-Aldrich	Cat #471283-100ML
Ethanolamine	Sigma-Aldrich	Cat #411000-100ML

Ultrapure water generated by Milli-Q® IQ 7000 Ultrapure Lab Water System	Millipore Sigma	https://www.emdmillipore.com
Cell culture media and related chemicals		
Dulbecco's phosphate-buffered saline (DPBS), no calcium, no magnesium	Thermo Fisher	Cat #14190144
Dulbecco's phosphate-buffered saline (DPBS), calcium, magnesium	Thermo Fisher	Cat #14040133
TransIT-LT1	Mirus Bio	Cat #MIR2306
Lipofectamine™ LTX with PLUS™ reagent	Thermo Fisher	Cat #12343593
Blasticidin	Invivogen	Cat #ant-bl-1
Geneticin™ Selective Antibiotic (G418 Sulfate)	Thermo Fisher	Cat #10131035
Trypsin-EDTA (0.25%), phenol red	Thermo Fisher	Cat #25200114
Fetal Bovine Serum (FBS), qualified, heat inactivated, United States	Thermo Fisher	Cat #S11550H
GIBCO™ FBS (AFM assay)	Fisher Scientific	Cat #11570506
Dulbecco's modified Eagle medium (DMEM)	Thermo Fisher	Cat #11965118
Ham's F-12 Nutrient Mix	Thermo Fisher	Cat #11765054
Ham's F-12 Nutrient Mix (AFM assay)	Sigma-Aldrich	Cat #N4888-500ML
Joklik's modified Eagle's minimal essential medium (JMEM)	United States Biological	Cat #M3867
Neurobasal medium	Thermo Fisher	Cat #21103049
B-27 supplement	Thermo Fisher	Cat #17504044
GIBCO™ L-glutamine	Thermo Fisher	Cat #A2916801
Penicillin-streptomycin (5,000 U/mL)	Thermo Fisher	Cat #15070063
Penicillin-streptomycin (AFM assay)	Sigma-Aldrich	Cat #P4333-100ML
Normocin (AFM assay)	InvivoGen	Cat #ant-nr-1
Amphotericin B solution	Sigma-Aldrich	Cat #A2942-50ML
Corning™ CellStripper Dissociation Reagent	Fisher Scientific	Cat #MT25056CI
32% Paraformaldehyde (PFA) aqueous solution	Electron Microscopy Sciences	Cat #15714
Methanol	Fisher Scientific	Cat #A412-500
Equipment		
LSR II Flow Cytometer	BD	https://www.bdbiosciences.com

Lionheart FX Automated Microscope	BioTek	https://www.agilent.com
TissueLyser LT	QIAGEN	Cat #85600
Stainless Steel Beads, 5 mm	QIAGEN	Cat #69989
Odyssey CLx Imager	LI-COR	https://www.licor.com/bio
UV radiation and ozone (UV-O)	Jetlight	https://www.jelight.com
ForceRobot300	JPK	https://www.jpk.com
NanoScope Multimode 8	Bruker	https://www.bruker.com
MSCT-D cantilevers	Bruker	https://www.brukerafmprobes.com
Zeiss Observer Z.1 epifluorescence microscope	Zeiss	https://www.zeiss.com
Bioscope Resolve AFM	Bruker	https://www.bruker.com
PFQNM-LC cantilevers	Bruker	https://www.brukerafmprobes.com
Gold-coated model surfaces	Silicon wafer: Siegert Wafer Company; Gold pellets: Neyco	Gold pellets: cat #AU3X6
OCTET® BLI	Sartorius	https://www.sartorius.com
OCTET® AR2G biosensors	Sartorius	https://www.sartorius.com
OCTET® NTA biosensors	Sartorius	https://www.sartorius.com
Mice and inoculation-related materials		
C57BL/6J mice	The Jackson Laboratory	Cat #000664
129S4/SvJaeJ mice	The Jackson Laboratory	Cat #009104
Hybrid C57BL/6J x 129S4/SvJaeJ mice	Current study	N/A
Formalin (10% in phosphate buffer)	Fisher Scientific	Cat #SF100-4
Syringe with BD Luer-Lok™ Tip	BD	Cat #309628
Syringe needle 30G	BD	Cat #305106
Hamilton syringe (Model 702 LT SYR)	Hamilton Company	Cat #80401
CRISPR-KO sgRNA sequences		
mNRP1 sgRNA1 5’ CTCTGACTATGAGACACATG 3’	Previous study[71]	N/A
mNRP1 sgRNA2 5’ CAAGACTCGAATCCTCCCGG 3’		
Software and Algorithms		
Gen5 software, v3.12	BioTek	https://www.agilent.com
CLC Genomics Workbench 22	QIAGEN	https://www.qiagen.com/

GraphPad Prism 10	GraphPad Software	https://www.graphpad.com
FlowJo v10.8.1	BD	https://www.flowjo.com
ImageJ	ImageJ	https://imagej.net
NanoScope software v9.1	Bruker	N/A
JPK Data Processing v6.1.149	JPK	N/A
NanoScope analysis software v1.7	Bruker	N/A
OriginPro 2021, v9.8.0.200	OriginLab	N/A
NanoScope software v9.2	Bruker	N/A
Gwyddion v2.58	Gwyddion	http://gwyddion.net
ZEN (blue edition) v3.2	Zeiss	https://www.zeiss.com
OCTET® BLI Discovery v12.2.2.20	Sartorius	N/A
OCTET® Analysis Studio v v12.2.2.26	Sartorius	N/A
Pymol	Pymol	https://pymol.org
UCSF Chimera	RBVI, UCSF	https://www.cgl.ucsf.edu/chimera
HDOCK Server	Huang Lab	http://hdock.phys.hust.edu.cn
BioRender	BioRender	https://www.biorender.com

[a]Not applicable.

523 **EXPERIMENTAL MODEL AND SUBJECT DETAILS**

524

525 **Cell lines and primary cells**

526 CHO, BV2, and BHK-T7 cells were maintained at 37°C in 5% CO_2 in completed Ham's
527 F-12 medium, DMEM, and DMEM, respectively. F-12 and DMEM media were
528 supplemented to contain 10% FBS, 2 mM L-glutamine, 100 U/ml penicillin/streptomycin,
529 and 250 ng/ml amphotericin B. T7 polymerase-expressing BHK-T7 cells were
530 maintained in DMEM medium supplemented to contain 1 mg/ml Geneticin. Spinner-
531 adapted L929 cells were maintained in JMEM supplemented to contain 5% FBS, L-
532 glutamine, penicillin/streptomycin, and amphotericin B in suspension (35°C, ambient
533 CO_2) or monolayer (37°C, 5% CO_2) cultures. Primary neurons were isolated from
534 cortices of E15.5 murine embryos and cultivated in neurobasal medium supplemented
535 to contain B-27 supplement as described previously.[27,72]

536

537 **Mice**

538 C57BL/6J x 129sv mice were maintained in a specific-pathogen-free vivarium or animal
539 biosafety level 2^+ ($ABSL2^+$) facility at a macroenvironmental temperature range of 68 to
540 76°F (20 to 24.4°C) and a relative humidity range of 35% to 55% with a 12 h/12 h
541 light/dark cycle. Mice were anesthetized with inhaled isoflurane.

542

543 **Viruses**

544 Recombinant reoviruses were recovered using plasmid-based reverse genetics by
545 transfecting cDNAs encoding viral gene segments into BHK-T7 cells as described

546 previously.[73] Mutant reovirus plasmids were engineered using site-directed
547 mutagenesis. Reovirus propagation, purification, plaque assay to determine infectious
548 units, fluorescent labelling, and ISVP preparation were conducted as described
549 previously.[27]
550
551 **METHOD DETAILS**
552
553 **CRISPR knockout**
554 BV2 cells were transfected with either empty CRISPR-KO transfer vector
555 (lentiCRISPRv2-blast) or vector encoding mNRP1-specific sgRNAs using Transit-LT1
556 according to the manufacturer's instructions. At 48 h post-transfection (hpt), cells were
557 selected with medium supplemented to contain 4 μg/ml blasticidin for 6 days. Surviving
558 cells were used to assess NRP1 expression and susceptibility to reovirus infection.
559
560 **Transient expression of receptor cDNAs**
561 CHO cells were transfected with receptor cDNAs using Transit-LT1 according to the
562 manufacturer's instructions and incubated for 48 h prior to analysis of reovirus binding
563 and infection.
564
565 **Reovirus binding assay**
566 Reovirus binding assays were conducted as described previously.[27] Purified virions of
567 strain T3DSA- (σ1 R202W/T249I) or T1LSA- (σ1 S370P/Q371E) were labelled with
568 Alexa Fluor 647 as described previously.[27] Cells were nonenzymatically dissociated with

569 CellStripper and either adsorbed with fluorescently-labelled reovirus (2×10^5 virions/cell)
570 or receptor-specific antibodies (PE- or APC-conjugated) at 4°C for 1 h. After virus or
571 antibody adsorption, cells were washed extensively with PBS and fixed with 2% PFA.
572 For antibody-blockade assays, CHO cells were incubated with NRP1-specific antibody
573 or isotype IgG at 4°C for 1 h prior to virus adsorption. Reovirus binding to CHO cells
574 was assessed by flow cytometry and quantified using FlowJo software.
575
576 **Reovirus infectivity assay**
577 CHO cells were transfected with receptor cDNAs as described previously.[27] Cells were
578 adsorbed with reovirus virions or ISVPs at various MOIs at 37°C for 1 h. The inoculum
579 was removed and replaced with Ham's F-12 medium supplemented to contain 2% FBS.
580 At 24 h post-adsorption (hpa), cells were fixed with ice-cold methanol, and viral infection
581 was detected by indirect immunofluorescence assay (IFA). For antibody- or VEGF-
582 blockade assays, CHO cells were incubated with NRP1-specific antibody or
583 recombinant mVEGF164 at 37°C for 1 h prior to reovirus adsorption. Isotype IgG was
584 used as a negative control for NRP1-specific antibody. For CendR-inhibitor treatment,
585 CHO cells were incubated with furin inhibitors CMK or Hexa-D-arginine or NRP1 b1
586 inhibitor EG 00229 at 37°C prior to reovirus adsorption. For receptor-competition
587 assays, the reovirus inoculum was pre-incubated with protein G beads, which were pre-
588 coated with 2.5 μg of recombinant NRP1-Fc or isotype IgG, prior to adsorption.
589 Cultivated murine primary neurons (7 days post-isolation) were adsorbed with
590 reovirus at 37°C for 1 h. For antibody-blockade assays, primary neurons were incubated
591 with NRP1-specific antibody or isotype IgG prior to adsorption with reovirus at 37°C for

592 1 h. At 24 hpa, neurons were fixed with 4% PFA in PBS at RT for 30 min, permeabilized
593 with 1% Triton X-100 in PBS at RT for 20 min, and blocked with PBS containing 5%
594 BSA (5% PBS-BSA) at RT for 30 min. Viral infection was detected by IFA.
595 Reovirus IFA was conducted using rabbit polyclonal reovirus-specific antiserum
596 (1:3000 dilution) and Alexa Fluor 488-conjugated goat anti-rabbit secondary antibody
597 (1:500 dilution). Antibodies were diluted in PBS containing 1% BSA (1% PBS-BSA).
598 Nuclei were stained with DAPI. Cells were imaged using a Lionheart FX fluorescence
599 microscope. Quantification of reovirus CHO cell infection was automated using Gen5
600 software (reovirus positive cells divided by total cells). Reovirus-infected neurons were
601 enumerated using the Cell Counter plugin of ImageJ software.
602
603 **Reovirus replication assays**
604 L929 cells or primary neurons were adsorbed with reovirus at 37°C for 1 h. The
605 inoculum was removed and replaced with fresh medium. Cells and supernatants were
606 harvested together at 24, 48, and 72 hpa by freezing. Titers in cell lysates were
607 determined by plaque assay as previously described.[27]
608
609 ***In vitro* precipitation assay**
610 Pierce™ protein G magnetic beads (15 µl/sample) were washed with PBS
611 supplemented to contain 0.02% Tween-20 (0.02% PBST) and incubated with 2.5 µg
612 recombinant Fc-tagged NRP1 or IgG isotype in PBS at RT for 1 h. Protein-coupled
613 beads were washed with 0.02% PBST and incubated with reovirus virions or ISVPs ($5 \times$
614 10^{10} particles) in PBS at RT for 1 h. Beads were washed twice with 0.02% PBST, and

615 bead-bound proteins were released and heat-denatured using 2x Laemmli loading
616 buffer. For σ3-NRP1 interaction studies, NRP1-coupled beads were incubated with 1 μg
617 of recombinant T3D σ3 protein. To eliminate nonspecific interactions, 0.5% PBST was
618 used as a binding and washing buffer, and σ3-bound beads were washed six times
619 before heat-denaturation. Input (50%) and bead-bound proteins were resolved by SDS-
620 PAGE, and gels were stained using the Colloidal Blue Staining Kit according to the
621 manufacturer's instructions. Protein gels were scanned using an Odyssey CLx Imager,
622 and fluorescence intensity of protein bands was quantified using Image Studio software.
623

624 **Structural analysis**

625 The following protein structures were acquired from the RCSB Protein Data Bank
626 (PDB): reovirus particle, 2CSE; virion sub-structures, 6XF8 and 7ELL; λ2 pentamer,
627 7YFE; mNRP1 a1-b2 extracellular region, 4GZ9; and hNRP1 c domain, 5L73. The
628 peripentameric subunit formed by λ2 and $\mu1_3\sigma3_3$ was generated by superimposing two
629 substructures (6XF8 and 7ELL) using UCSF Chimera software. Protein structures were
630 rendered and visualized using PyMOL software. *In silico* protein interactions were
631 simulated using the HDOCK program with the constraints of capsid protein residues,
632 including polymorphic residues in λ2 region I-II and σ3 patch I-III, found to be required
633 for reovirus-NRP1 binding. The following NCBI GenBank accession numbers were used
634 to analyze reovirus L2 and S4 sequences: T1L L2 (AAK57507.1); T3D L2
635 (ABP48914.1); T1L S4 (CAA43783.1); and T3D S4 (ABP48922.1). Amino acid
636 polymorphisms in T1L and T3D capsid proteins were identified using the alignment
637 function in CLC Genomics Workbench software.

638

639 **Functionalization of AFM tips**

640 AFM tips were functionalized as described previously.[74,75] *Amino-functionalization*:
641 Briefly, MSCT (for model surface experiments) or PFQNM-LC (for live cell experiments)
642 cantilevers were washed with chloroform for 5 min and cleaned with UV-O for 15 min. A
643 desiccator was flooded with argon gas, and tips were placed inside the desiccator.
644 APTES (30 µL) and triethylamine (10 µL) were added separately into two trays within
645 the desiccator, which was subsequently closed. After incubation for 2 h, trays were
646 removed, and the desiccator was flooded with argon gas for 10 min. APTES coating on
647 the tips were left to cure for at least 2 days. *Tip coupling with flexible PEG linkers*: Tips
648 were immersed for 2 h in a solution containing Ald-Ph-PEG_{24}-NHS ester (3.3 mg) in
649 chloroform (0.5 ml) and triethylamine (30 µl) and then cleaned three times for 5 min in
650 chloroform. After letting the tips dry, the tips were placed on Parafilm in a Petri dish and
651 stored in an ice box. *Virus linkage:* Virus (10^8 particles of T3DSA- [σ1 R202W/T249I]) in
652 100 µl was added to tips, and 2 µl of freshly prepared sodium cyanoborohydride
653 solution (~ 6% [wt/vol] in 0.1 M NaOH) was added to the virus droplet. Tips were
654 incubated at 4°C for 1 h. Reactions were quenched by adding 5 µL of ethanolamine (1
655 M [pH 8.0]) to the droplet and incubating at 4°C for 10 min. Tips were rinsed three times
656 in ice-cold virus storage buffer (150 mM NaCl, 15 mM $MgCl_2$, and 10 mM Tris [pH 7.4] in
657 MilliQ water).[34] Tips were stored individually in virus storage buffer at 4°C until use.

658

659 **Preparation of NRP1-coated AFM surfaces**

660 His-tagged mNRP1 or hNRP1 proteins were grafted onto gold-coated model surfaces
661 by NTA-His_6 binding chemistry as described previously.[76] Surfaces were rinsed with
662 ethanol, dried with a low nitrogen flow, and cleaned with UV-O for 15 min. Surfaces
663 were incubated in an ethanol solution containing 0.05 mM NTA-terminated (10%) and
664 PEG-terminated (90%) alkanethiols. After incubation overnight, the surfaces were
665 rinsed with ethanol, dried with nitrogen gas, and incubated in a 40 mM aqueous solution
666 of $NiSO_4$ (pH 7.2) for 1 h. Surfaces were rinsed with MilliQ water, dried with nitrogen
667 gas, placed on a Teflon surface, and incubated with recombinant mNRP1 or hNRP1
668 (0.1 mg/ml) for 1 h. Surfaces were rinsed ~ 10 times with PBS and kept hydrated at 4°C
669 until use.
670
671 **FD-based AFM using model surfaces**
672 Force-distance (FD) curve-based AFM experiments were conducted using virus-
673 functionalized MSCT-D probes in virus buffer at room temperature. Force-Robot300 or
674 NanoScope Multimode 8 were used to conduct experiments in force-volume mode. The
675 thermal tune method[77] was used to calculate cantilever spring constants, which ranged
676 from 0.02 to 0.04 N/m. NRP1-grafted model surfaces were mounted on a piezoelectric
677 scanner using a magnetic carrier. For all AFM experiments, areas of 5 × 5 μm (with 32 ×
678 32-pixel resolution) were scanned (corresponding to 1,024 FD curves) with a ramp size
679 set to 500 nm. The maximum force was set to 500 pN, and the approach velocity was
680 maintained at 1 μm/s. Binding frequency (BF) was calculated as the percentage of
681 analyzed curves that displayed specific adhesion events.

682 Surface-blocking experiments were conducted as independent controls to ensure
683 specific interactions between virus and sample. Measurements were collected before
684 and after adding 50 µg/ml of anti-mNRP1 mAb or 100 µg/ml of hVEGF165 to
685 independent samples. For all blocking experiments, the same sample area was probed
686 several times using the same tip.
687 To probe a wide range of loading rates, dynamic force spectroscopy (DFS)
688 experiments were conducted with no surface delay and by varying the retraction
689 velocities (0.1, 0.2, 1, 5, 10, and 20 µm/s). Kinetic on-rate (k_{on}) measurements were
690 made using different hold times (0, 50, 100, 150, 250, 500 and 1000 ms), which allowed
691 the tip to stay in contact with the surface for different intervals.
692 Depending on the instrument used, either JPK Data Processing or NanoScope
693 analysis software was employed for analysis. For DFS data, FD-curves were fit with the
694 worm-like chain model for polymer extension.[78] Loading rates were determined using
695 the slope of the force-time curves and rupture forces were extracted. The results were
696 displayed in DFS plots using Origin software, which also was used to fit histograms of
697 rupture force distributions for distinct loading rate (LR) ranges, applying various force
698 spectroscopy models, as described.[79,80] For kinetic on-rate analyses, BFs were
699 determined for different hold times, and data were fit and K_D calculated as described.[81]
700
701 **Preparation of cells for live-cell AFM studies**
702 CHO cells were cultivated at 37°C in a humidified atmosphere with 5% CO_2 in Ham's F-
703 12 medium supplemented to contain 10% FBS, penicillin, streptomycin, normocin, and
704 L-glutamine. Cells were seeded into slide-bottom microdishes, incubated for 24 h, and

705 transfected with pcDNA3.1(+)-mNRP1-IRES-GFP plasmid using Lipofectamine LTX and
706 Plus reagent according to the manufacturer's instructions. Medium was replaced ~ 6 h
707 after transfection. Cells were incubated overnight and gently rinsed five times with fresh
708 medium prior to imaging in Ham's F-12 medium.
709
710 **FD-based AFM and correlative imaging using living cells**
711 FD-based AFM was conducted using a Bioscope Resolve AFM, operated in PeakForce
712 QNM mode, equipped with a 150-µm piezoelectric scanner. Correlative fluorescence
713 images were obtained using an inverted epifluorescence microscope coupled to the
714 AFM. The cell-culture chamber was maintained at 37°C ± 1°C and infused at 0.1 l/min
715 with a gas mixture supplemented with 5% CO_2 and 95% relative humidity. Vacuum,
716 incorporated into the AFM sample plate, was used to stabilize the cell dish. PFQNM-LC
717 cantilevers were used with pre-calibrated spring constants. Deflection sensitivity of the
718 cantilevers was calculated using the thermal-tune method. AFM images were collected
719 by probing an area of 22 to 30 µm at imaging forces of 500 pN and a scan frequency of
720 0.125 Hz. The sample was scanned using 256 pixels per line (256 lines). Cantilevers
721 were oscillated at 0.25 kHz in PeakForce tapping mode, with an amplitude of 750 nm.
722 Fluorescent images were collected using standard GFP and DIC settings. In a subset of
723 experiments, correlative images were acquired before and after adding hVEGF165 (at
724 0.5 µg/ml) by scanning the same area using identical experimental parameters.
725 NanoScope analysis software and Origin software were used to analyze FD-curves
726 showing adhesion events. Loading rates were determined using the slope of the force-
727 time curves. AFM images were analyzed using NanoScope analysis software and

728 Gwyddion. Binding frequency was calculated by pixel counting using ImageJ. Optical
729 images were analyzed using ZEN (blue edition) software. Force peak predictions were
730 estimated using Origin software by visually intercepting the Williams-Evans prediction
731 curves, which is based on model surface data, with the LR average of living cell
732 data.[44,82,83]
733
734 **Biolayer interferometry**
735 Amine-reactive biosensors were hydrated in PBS for 10 min, after which an initial
736 baseline was assessed in PBS for 60 s. Recombinant reovirus σ3 protein (10 μg/ml)
737 was grafted onto the sensor via an NHS/EDC coupling step (300 s), followed by
738 quenching with ethanolamine (300 s). After a second PBS baseline (60 s), the sensor
739 was dipped in solutions containing recombinant mNRP1 or hNRP1 at different
740 concentrations (13, 26, and 52 nM, respectively) for 20 min. Dissociation steps were
741 conducted in PBS for 10 min. As a control, interactions between mNRP1 or hNRP1 and
742 σ3 were investigated in the presence of hVEGF165. After an initial PBS baseline (60 s),
743 Ni-NTA biosensors were loaded with recombinant His-tagged mNRP1 or hNRP1 (10
744 μg/ml) for 10 min. Following a second PBS baseline, sensor was dipped in solution
745 containing VEGF165 (10 μg/ml) for 10 min. After a 300-s dissociation step in PBS, the
746 sensors were immersed in a σ3 solution (2 μg/ml) for 10 min. Lastly, a final baseline in
747 PBS was determined for 300 s. All measurements were conducted at 25°C and shaker
748 speed at 1000 rpm. For kinetic assessments, the association and dissociation sections
749 of the curve were fit with a Langmuir 1:1 stoichiometric model to obtain the dissociation
750 constant (K_D) using Octet Analysis software.

751

752 **Reovirus infections of mice**

753 Neonatal (2-day-old) C57BL/6J x 129sv hybrid mice (body weight = 1.5 to 2.3 g) were
754 inoculated with 5 µl of virus diluted in PBS using a 30-gauge needle attached to a
755 Hamilton syringe. For intracranial (IC) inoculations, mice were inoculated in the right
756 cerebral hemisphere and either euthanized at various intervals (for viral replication and
757 histology studies) or euthanized when found to be moribund (for viral virulence studies).
758 Mouse brains were hemisected along the longitudinal fissure. Right-brain hemispheres
759 were processed for determination of viral titers, and left-brain hemispheres were fixed in
760 10% neutral-buffered formalin (NBF) for immunohistochemistry. For intramuscular (IM)
761 inoculations, mice were inoculated in the right quadriceps muscle. Tissue samples were
762 collected into 1 mL of PBS. Tissues and whole blood were frozen and thawed twice and
763 homogenized using a TissueLyser LT and stainless-steel beads. Viral titers in tissue
764 homogenates were determined by plaque assay. Inoculated mice were monitored daily
765 for signs of disease, including lethargy, seizures, and paralysis. Moribund mice with any
766 of these symptoms or mice with ≥ 25% body weight loss were euthanized. Viral titers of
767 inocula were confirmed by plaque assay to be within 3-fold of the intended dose.

768

769 **Immunohistochemistry**

770 Immunohistochemistry of brain sections was conducted as described previously.[27] Left-
771 brain hemispheres collected from intracranially inoculated mice were fixed using 10%
772 NBF for 24 h and transferred to fresh NBF solution. Tissue samples were embedded in
773 paraffin and divided into 5 µm-thick sections. Sections were submerged in xylene at RT

774 for 5 min to remove paraffin, hydrated by serial passage in dilutions of ethanol (100%,
775 95%, 70%, and 50%) at RT for 5 min, and rinsed with distilled water. Antigen retrieval
776 was accomplished by incubating sections in sodium citrate buffer (10 mM sodium
777 citrate, 0.05% Tween-20, pH = 6) at 95-100°C for 45 min. Sections were incubated with
778 5% PBS-BSA at RT for 1 h and rabbit reovirus-specific polyclonal antiserum diluted 1:
779 3,000 in 1% PBS-BSA at RT for 1 h. After three washes with PBS containing 0.1%
780 Tween-20 and 0.1 M glycine, sections were incubated with Alexa Fluor 488-conjugated
781 goat anti-rabbit secondary antibody diluted 1: 500 in 1% PBS-BSA and washed three
782 times with PBS containing 0.1% Tween-20 and 0.1 M glycine. Nuclei were stained with
783 DAPI. Tissue sections were mounted with Aqua-Poly/Mount on glass coverslips
784 overnight at RT and scanned using a Lionheart FX fluorescence microscope.
785

786 **FIGURE LEGENDS**

787

788 **Figure 1. mNRP1 promotes reovirus binding and infection**

789 (A) Reovirus infection of genetically modified BV2 cells. Cells expressing mNRP1-
790 specific CRISPR-KO sgRNAs were adsorbed with reovirus strain T1L at a multiplicity of
791 infection (MOI) of 1000 PFU/cell and strain T3D at an MOI of 10 PFU/cell. Empty
792 sgRNA vector was used as a negative control.
793 (B-G) CHO cells were transfected with the receptor cDNAs shown. hJAM-A was used
794 as a positive control; hCAR and empty vector (EV) were used as negative controls. (B)
795 Reovirus infection of receptor-expressing cells. (C) Reovirus binding to receptor-
796 expressing cells. Cells were adsorbed with fluorescent T1LSA- or T3DSA-. (D-E) Cells
797 were preincubated with mNRP1-specific mAb or isotype IgG prior to reovirus
798 adsorption. Effect of mNRP1-specific mAb on (D) T3DSA- binding and (E) T3D
799 infection. (F) Effect of VEGF on mNRP1-mediated T3D infection. Cells were
800 preincubated with murine VEGF164 (mVEGF164) prior to reovirus adsorption. (G)
801 Effect of recombinant mNRP1 ectodomain on T3D infection. The viral inoculum was
802 incubated with recombinant mNRP1-Fc or IgG-coupled protein G beads prior to
803 adsorption. (C-D) Virus binding was assessed by flow cytometry. (B, E-G) Cells were
804 adsorbed with reovirus at a MOI of 10 PFU/cell.
805 (A-B, E-G) Infectivity was quantified by indirect immunofluorescence assay (IFA).
806 Experiments were conducted in quadruplicate (A, C-D) or triplicate (B, E-G). Mean
807 values are shown. Error bars indicate standard deviation (SD). (A) Two-way ANOVA
808 with Holm-Sidak's test. (D-G) One-way ANOVA with Tukey's test. ****, $P < 0.0001$.

809

810 **Figure 2. Biophysics of reovirus-NRP1 interactions**

811 (A) Binding of reovirus particles to NRP1 assessed by precipitation assay. Protein G
812 beads coupled with recombinant Fc-tagged mNRP1, hNRP1, or IgG isotype were
813 incubated with T3DSA- or T1LSA- virions. Input (50%) and bound proteins were
814 resolved by SDS-PAGE and stained for total protein.

815 (B-K) Reovirus-NRP1 binding thermodynamics on model surfaces (B–E) and living cells
816 (F-K). (B) Experimental schematic for probing reovirus binding to a recombinant
817 mNRP1-coated model surface. (C) Binding frequency on model surfaces before and
818 after hVEGF165 or mNRP1-specific mAb treatment. One data point represents the
819 binding frequency obtained for one map consisting of 1,024 FD curves. (D) Dynamic
820 force spectroscopy (DFS) plot of the distribution of average rupture forces across
821 discrete loading rate ranges. Solid line, Bell-Evans fit. $n = 2597$. (E) Binding frequency
822 as a function of the contact time between a T3DSA- virion-functionalized tip with the
823 mNRP1-coated surface. Least-squares fit of the data to a mono-exponential decay
824 model (black line, $r^2 = 0.99$) provides the average binding kinetic on-rate (k_{on}). The Bell-
825 Evans fit provides k_{off} and x_u values, and the K_D is calculated using k_{off}/k_{on}.

826 (F) Experimental schematic for probing reovirus binding on living CHO cells. (G)
827 Representative DIC and fluorescence images, height, and adhesion maps. Data were
828 collected by scanning the boxed area (top) containing mNRP1$^+$ and mNRP1$^-$ cells. The
829 maps correspond to recorded binding events are indicated by bright pixels. (H) Binding
830 frequency of T3DSA- on living cells. (I) T3DSA- binding to living cells before and after
831 hVEGF165 treatment. (J) DFS plot of T3DSA- interactions with mNRP1 on living cells
832 (blue; $n = 1247$). Model surface data (D) were incorporated (gray). Solid line (I): Bell-

833 Evans fit; dashed line (II to VI): Williams-Evans prediction. (K) Force distribution of the
834 T3DSA- interaction with mNRP1 on living cells. Estimated rupture force peaks
835 corresponding to mono- (I) or multi-valent interactions (II to VI) are shown.
836 (C-E, H-K) Mean values are shown. Error bars indicate SD. All data are representative
837 of at least $n = 3$ independent experiments. (C and H) Two-sided Student's t-test. (I)
838 Two-way ANOVA with Turkey's test. *, $P < 0.05$; **, $P < 0.01$; ***, $P < 0.001$; ****,
839 $P < 0.0001$.

840 **Figure 3. Reovirus-NRP1 interactions require multiple NRP1 extracellular domains**

841 (A) Schematic of mNRP1 (blue) and hNRP1 (red) wild-type (WT) and chimeric
842 receptors. PM, plasma membrane.

843 (B-D, F-H) CHO cells were transfected with the receptor cDNAs shown. (B) Ectopic
844 expression of chimeric receptors was detected by NRP1-specific antibody. (C) Reovirus
845 T3DSA- binding to chimeric receptor-expressing cells. (D) Reovirus T3D infection of
846 chimeric receptor-expressing cells following adsorption at an MOI of 10 PFU/cell.

847 (E) Schematic of mNRP1 ectodomain deletion constructs.

848 (F) Ectopic expression of mutant receptors was detected by mNRP1-specific mAb. (G)
849 Reovirus T3DSA- binding to mutant receptor-expressing cells. (H) Reovirus T3DSA-
850 infection of mutant receptor-expressing cells following adsorption at an MOI of 30
851 PFU/cell.

852 Experiments were conducted in triplicate (D, H) or quadruplicate (B-C, F-G). Mean
853 values are shown. Error bars indicate SD. (C-D, G-H) One-way ANOVA with Turkey's
854 test. *, $P < 0.05$; **, $P < 0.01$; ****, $P < 0.0001$.

855 **Figure 4. Multiple reovirus capsid proteins are required for interactions with NRP1**

856 (A) Panel of T1L x T3D reassortant viruses.

857 (B-D) CHO cells were transfected with the receptor cDNAs shown. (B-C) Infection of

858 mNRP1-expressing cells by reassortant viruses following adsorption at an MOI of 5

859 PFU/cell. (D) Infection of mNRP1-expressing cells by T3DSA- virions and ISVPs

860 following adsorption at an MOI of 2 x 10^4 particles/cell.

861 (E) Binding of T3DSA- virions and ISVPs to recombinant mNRP1.

862 (F) Binding of T3D σ3 to recombinant mNRP1.

863 (E-F) Interactions were assessed using a precipitation assay. Protein G beads coupled

864 with Fc-tagged mNRP1 or IgG isotype were incubated with either viral particles or

865 recombinant σ3.

866 (G-H) Biolayer interferometry (BLI) sensograms depicting association and dissociation

867 trace of T3D σ3 with either mNRP1 (G) or hNRP1 (H). Blue lines represent an

868 independent experiment with the concentrations shown of recombinant NRP1 and

869 green lines represent the fit. Isotherms were fit using 1:1 model to estimate K_D.

870 (B-D) Experiments were conducted in triplicate. Mean values are shown. Error bars

871 indicate SD.

872 **Figure 5. Capsid turret protein λ2 contributes to NRP1 binding and is required for**
873 **NRP1-mediated infectivity**
874 (A) Surface-rendered structure of the reovirus capsid and the peripentameric subunit
875 structure formed by λ2 and $\mu1_3\sigma3_3$ (representative subunit outlined on the left,
876 expanded on the right). The structure of the T3D virion was acquired from the Protein
877 Data Bank (PDB ID 2CSE). The peripentameric subunit was generated by
878 superimposing two substructures (PDB IDs 6XF8 and 7ELL).
879 (B, C) Domain organization (B) and surface rendering (C) of λ2 protein (PDB, ID 6XF8).
880 IBMs are depicted in cyan; T1L-T3D polymorphic residues are shown in magenta.
881 Numbered residues were exchanged.
882 (D) Polymorphic residues in λ2 regions I and II chosen for substitution.
883 (E) Infection of receptor-expressing cells by λ2 mutants. T3D mutants, MOI of 5
884 PFU/cell; T3DSA- mutants, MOI of 30 PFU/cell; and T1LSA- mutants, MOI of 100
885 PFU/cell.
886 (F-G) Binding of WT T3DSA- or λ2 mutants to mNRP1 assessed by precipitation assay.
887 Representative gel images (F) and quantification (G) are shown. Relative binding
888 efficiency was calculated by normalizing band intensity of the capsid μ1 or σ proteins to
889 that of the corresponding input level and subsequently compared with the levels for WT
890 T3DSA-.
891 (E-G) Assays were conducted in triplicate. Mean values are shown. Error bars indicate
892 SD. (G) One-way ANOVA with Turkey's test. *, $P < 0.05$; ***, $P < 0.001$.****, $P < 0.0001$.

893 **Figure 6. Protomers of outer-capsid protein σ3 are engaged in interactions with**
894 **NRP1**

895 (A) Surface-rendered (left) or ribbon-tracing (right, partial) view of outer-capsid complex
896 of λ2 and $\sigma3_3\mu1_3$ (PDB ID: 6XF8). T1L-T3D polymorphic residues within λ2 region I and
897 II, σ3, and μ1 are depicted in magenta; IBM (KGE) is shown in cyan. Dashed ovals
898 indicate three patches of polymorphic residues in σ3. Polymorphic σ3 residues in these
899 patches are indicated on the ribbon diagram in (A) and summarized in (B).

900 (C) Design of T3D σ3 mutants to define the structural basis of reovirus-NRP1
901 interactions.

902 (D) Infection of receptor-expressing cells by WT T3DSA- and σ3 mutants following
903 adsorption at an MOI of 30 PFU/cell.

904 (E) Binding of WT T3DSA- or σ3 mutants to mNRP1 assessed by precipitation assay.
905 (D-E) Mutants used for pathogenesis studies were highlighted.

906 (F) Design of T3D σ3 Patch III mutants to define the structural basis of reovirus-NRP1
907 interactions.

908 (G) Infection of receptor-expressing cells by T3DSA- and T1LSA- σ3 mutants following
909 adsorption at an MOI of 30 PFU/cell.

910 (H) Binding of WT T3DSA- or σ3 mutants to mNRP1 assessed by precipitation assay.

911 (E, H) Binding efficiency was calculated by normalizing band intensity of the viral μ1 and
912 σ proteins to that of the corresponding input level.

913 (D-H) Assays were conducted in triplicate. Mean values are shown. Error bars indicate
914 SD. (E, H) One-way ANOVA with Turkey's test. *, $P < 0.05$; **, $P < 0.01$; ***, $P <$
915 0.001.****, $P < 0.0001$.

916 **Figure 7. NRP1 contributes to reovirus dissemination and neurovirulence in mice**

917 (A) Effect of mNRP1-specific antibody blockade on reovirus infection of primary murine
918 cortical neurons. Neurons were preincubated with mNRP1-specific mAb or isotype IgG
919 and adsorbed with WT T3DSA- at an MOI of 20 PFU/cell.

920 (B) Replication of WT T3DSA- and NRP1-binding mutants in L929 cells following
921 adsorption at an MOI of 0.1 PFU/cell. NBM, NRP1-binding mutant.

922 (C) Infection of primary neurons by WT T3DSA- and NBMs.

923 (D) Replication of WT T3DSA- and NBMs following infection of primary neurons.

924 (A, C) Viral infectivity was quantified by IFA.

925 (E) Replication of WT T3DSA- and NBMs in mice following intracranial inoculation of
926 100 PFU/mouse. $n = 4$, 6, and 8 at 4, 6, and 8 DPI (WT); $n = 8$, 11, and 9 at 4, 6, and 8
927 DPI (NBM1); $n = 8$, 9, and 9 at 4, 6, and 8 DPI (NBM2).

928 (F) WT T3DSA- and NBMs virulence in mice following intracranial inoculation of 100
929 PFU/mouse.

930 (G) Replication of WT T3DSA- and NBMs in mice following intramuscular inoculation of
931 10^7 PFU/mouse. $n = 9$, 10, and 9 at 2, 4, and 8 DPI (WT); $n = 9$, 10, and 9 at 2, 4, and 8
932 DPI (NBM1); $n = 9$, 9, and 8 at 2, 4, and 8 DPI (NBM2).

933 (D, E, G) Viral replication was quantified by plaque assay.

934 (E and G) Each symbol indicates a single mouse. Mean values are shown. Error bars
935 indicate SD. Limit of detection (LOD) was shown with dash line. (A-D) Two-way ANOVA
936 with Holm-Sidak's test. (E, G) Multiple unpaired t tests. (F) Log-rank (Mantel-Cox) test.
937 *, $P < 0.05$; **, $P < 0.01$; ***, $P < 0.001$; ****, $P < 0.0001$.

938

939 **REFERENCES**

940 1. Raimondi, C., Brash, J.T., Fantin, A., and Ruhrberg, C. (2016). NRP1 function
941 and targeting in neurovascular development and eye disease. Prog Retin Eye
942 Res *52*, 64-83. 10.1016/j.preteyeres.2016.02.003.
943 2. Raimondi, C., and Ruhrberg, C. (2013). Neuropilin signalling in vessels, neurons
944 and tumours. Semin Cell Dev Biol *24*, 172-178. 10.1016/j.semcdb.2013.01.001.
945 3. Guo, H.F., and Vander Kooi, C.W. (2015). Neuropilin functions as an essential
946 cell surface receptor. J Biol Chem *290*, 29120-29126. 10.1074/jbc.R115.687327.
947 4. Chuckran, C.A., Liu, C., Bruno, T.C., Workman, C.J., and Vignali, D.A. (2020).
948 Neuropilin-1: a checkpoint target with unique implications for cancer immunology
949 and immunotherapy. J Immunother Cancer *8*. 10.1136/jitc-2020-000967.
950 5. Parker, M.W., Guo, H.F., Li, X., Linkugel, A.D., and Vander Kooi, C.W. (2012).
951 Function of members of the neuropilin family as essential pleiotropic cell surface
952 receptors. Biochemistry *51*, 9437-9446. 10.1021/bi3012143.
953 6. Balistreri, G., Yamauchi, Y., and Teesalu, T. (2021). A widespread viral entry
954 mechanism: the c-end rule motif-neuropilin receptor interaction. Proc Natl Acad
955 Sci U S A *118*. 10.1073/pnas.2112457118.
956 7. Daly, J.L., Simonetti, B., Klein, K., Chen, K.E., Williamson, M.K., Antón-Plágaro,
957 C., Shoemark, D.K., Simón-Gracia, L., Bauer, M., Hollandi, R., et al. (2020).
958 Neuropilin-1 is a host factor for SARS-CoV-2 infection. Science *370*, 861-865.
959 10.1126/science.abd3072.
960 8. Cantuti-Castelvetri, L., Ojha, R., Pedro, L.D., Djannatian, M., Franz, J., Kuivanen,
961 S., van der Meer, F., Kallio, K., Kaya, T., Anastasina, M., et al. (2020).

962 Neuropilin-1 facilitates SARS-CoV-2 cell entry and infectivity. Science *370*, 856-
963 860. 10.1126/science.abd2985.
964 9. Kielian, M. (2020). Enhancing host cell infection by SARS-CoV-2. Science *370*,
965 765-766. 10.1126/science.abf0732.
966 10. Martinez-Martin, N., Marcandalli, J., Huang, C.S., Arthur, C.P., Perotti, M.,
967 Foglierini, M., Ho, H., Dosey, A.M., Shriver, S., Payandeh, J., et al. (2018). An
968 unbiased screen for human cytomegalovirus identifies neuropilin-2 as a central
969 viral receptor. Cell *174*, 1158-1171.e1119. 10.1016/j.cell.2018.06.028.
970 11. Wang, H.B., Zhang, H., Zhang, J.P., Li, Y., Zhao, B., Feng, G.K., Du, Y., Xiong,
971 D., Zhong, Q., Liu, W.L., et al. (2015). Neuropilin 1 is an entry factor that
972 promotes EBV infection of nasopharyngeal epithelial cells. Nat Commun *6*, 6240.
973 10.1038/ncomms7240.
974 12. Lu, Z.Z., Sun, C., Zhang, X., Peng, Y., Wang, Y., Zeng, Y., Zhu, N., Yuan, Y.,
975 and Zeng, M.S. (2023). Neuropilin 1 is an entry receptor for KSHV infection of
976 mesenchymal stem cell through TGFBR1/2-mediated macropinocytosis. Sci Adv
977 *9*, eadg1778. 10.1126/sciadv.adg1778.
978 13. Dimitrov, D.S. (2004). Virus entry: molecular mechanisms and biomedical
979 applications. Nat Rev Microbiol *2*, 109-122. 10.1038/nrmicro817.
980 14. Maginnis, M.S. (2018). Virus-Receptor Interactions: The Key to Cellular Invasion.
981 J Mol Biol *430*, 2590-2611. 10.1016/j.jmb.2018.06.024.
982 15. Morizono, K., and Chen, I.S. (2011). Receptors and tropisms of envelope
983 viruses. Curr Opin Virol *1*, 13-18. 10.1016/j.coviro.2011.05.001.

984 16. Long, J.S., Mistry, B., Haslam, S.M., and Barclay, W.S. (2019). Host and viral
985 determinants of influenza A virus species specificity. Nat Rev Microbiol *17*, 67-
986 81. 10.1038/s41579-018-0115-z.
987 17. Lu, D., Shang, G., He, X., Bai, X.C., and Zhang, X. (2021). Architecture of the
988 Sema3A/PlexinA4/Neuropilin tripartite complex. Nat Commun *12*, 3172.
989 10.1038/s41467-021-23541-x.
990 18. Kschonsak, M., Johnson, M.C., Schelling, R., Green, E.M., Rougé, L., Ho, H.,
991 Patel, N., Kilic, C., Kraft, E., Arthur, C.P., et al. (2022). Structural basis for HCMV
992 pentamer receptor recognition and antibody neutralization. Sci Adv *8*, eabm2536.
993 10.1126/sciadv.abm2536.
994 19. Wrapp, D., Ye, X., Ku, Z., Su, H., Jones, H.G., Wang, N., Mishra, A.K., Freed,
995 D.C., Li, F., Tang, A., et al. (2022). Structural basis for HCMV pentamer
996 recognition by neuropilin 2 and neutralizing antibodies. Sci Adv *8*, eabm2546.
997 10.1126/sciadv.abm2546.
998 20. Chen, M., Wang, M.H., Shen, X.G., Liu, H., Zhang, Y.Y., Peng, J.M., Meng, F.,
999 Wang, T.Y., Bai, Y.Z., Sun, M.X., et al. (2022). Neuropilin-1 facilitates
1000 pseudorabies virus replication and viral glycoprotein B promotes its degradation
1001 in a furin-dependent manner. J Virol *96*, e0131822. 10.1128/jvi.01318-22.
1002 21. Knipe, D.M., and Howley, P.M. (2013). Fields virology, 6th Edition (Wolters
1003 Kluwer/Lippincott Williams & Wilkins Health).
1004 22. Kobayashi, T., Antar, A.A., Boehme, K.W., Danthi, P., Eby, E.A., Guglielmi, K.M.,
1005 Holm, G.H., Johnson, E.M., Maginnis, M.S., Naik, S., et al. (2007). A plasmid-

1006 based reverse genetics system for animal double-stranded RNA viruses. Cell
1007 Host Microbe *1*, 147-157. 10.1016/j.chom.2007.03.003.
1008 23. Roth, A.N., Aravamudhan, P., Fernández de Castro, I., Tenorio, R., Risco, C.,
1009 and Dermody, T.S. (2021). Ins and outs of reovirus: vesicular trafficking in viral
1010 entry and egress. Trends Microbiol *29*, 363-375. 10.1016/j.tim.2020.09.004.
1011 24. Sutherland, D.M., Aravamudhan, P., and Dermody, T.S. (2018). An orchestra of
1012 reovirus receptors: Still searching for the conductor. Adv Virus Res *100*, 223-246.
1013 10.1016/bs.aivir.2017.10.005.
1014 25. Bouziat, R., Hinterleitner, R., Brown, J.J., Stencel-Baerenwald, J.E., Ikizler, M.,
1015 Mayassi, T., Meisel, M., Kim, S.M., Discepolo, V., Pruijssers, A.J., et al. (2017).
1016 Reovirus infection triggers inflammatory responses to dietary antigens and
1017 development of celiac disease. Science *356*, 44-50. 10.1126/science.aah5298.
1018 26. Medina Sanchez, L., Siller, M., Zeng, Y., Brigleb, P.H., Sangani, K.A., Soto, A.,
1019 Engl, C., Laughlin, C.R., Rana, M., Van Der Kraak, L., et al. (2023). The gut
1020 protist tritrichomonas arnold restrains virus-mediated loss of oral tolerance by
1021 modulating dietary antigen-presenting dendritic cells. Immunity *56*, 1862-1875.
1022 10.1016/j.immuni.2023.06.022.
1023 27. Shang, P., Simpson, J.D., Taylor, G.M., Sutherland, D.M., Welsh, O.L.,
1024 Aravamudhan, P., Natividade, R.D.S., Schwab, K., Michel, J.J., Poholek, A.C., et
1025 al. (2023). Paired immunoglobulin-like receptor B is an entry receptor for
1026 mammalian orthoreovirus. Nat Commun *14*, 2615. 10.1038/s41467-023-38327-6.
1027 28. Konopka-Anstadt, J.L., Mainou, B.A., Sutherland, D.M., Sekine, Y., Strittmatter,
1028 S.M., and Dermody, T.S. (2014). The Nogo receptor NgR1 mediates infection by

1029 mammalian reovirus. Cell Host Microbe *15*, 681-691.
1030 10.1016/j.chom.2014.05.010.
1031 29. Aravamudhan, P., Guzman-Cardozo, C, Urbanek, K, Welsh, OL, Konopka-
1032 Anstadt, JL, Sutherland, DM, and Dermody, TS (2021). The murine neuronal
1033 receptor NgR1 is dispensable for reovirus pathogenesis. J Virol *96*, e00055-
1034 00022.
1035 30. Antar, A.A.R., Konopka, J.L., Campbell, J.A., Henry, R.A., Perdigoto, A.L.,
1036 Carter, B.D., Pozzi, A., Abel, T.W., and Dermody, T.S. (2009). Junctional
1037 adhesion molecule-A is required for hematogenous dissemination of reovirus.
1038 Cell Host Microbe *5*, 59-71. 10.1016/j.chom.2008.12.001.
1039 31. Barton, E.S., Forrest, J.C., Connolly, J.L., Chappell, J.D., Liu, Y., Schnell, F.J.,
1040 Nusrat, A., Parkos, C.A., and Dermody, T.S. (2001). Junction adhesion molecule
1041 is a receptor for reovirus. Cell *104*, 441-451. Doi 10.1016/S0092-8674(01)00231-
1042 8.
1043 32. Stencel-Baerenwald, J., Reiss, K., Blaum, B.S., Colvin, D., Li, X.N., Abel, T.,
1044 Boyd, K., Stehle, T., and Dermody, T.S. (2015). Glycan engagement dictates
1045 hydrocephalus induction by serotype 1 reovirus. mBio *6*, e02356-02314.
1046 10.1128/mBio.02356-14.
1047 33. Frierson, J.M., Pruijssers, A.J., Konopka, J.L., Reiter, D.M., Abel, T.W., Stehle,
1048 T., and Dermod, T.S. (2012). Utilization of sialylated glycans as coreceptors
1049 enhances the neurovirulence of serotype 3 reovirus. J Virol *86*, 13164-13173.
1050 10.1128/Jvi.01822-12.

1051 34. Koehler, M., Aravamudhan, P., Guzman-Cardozo, C., Dumitru, A.C., Yang, J.,
1052 Gargiulo, S., Soumillion, P., Dermody, T.S., and Alsteens, D. (2019). Glycan-
1053 mediated enhancement of reovirus receptor binding. Nat Commun *10*, 4460.
1054 10.1038/s41467-019-12411-2.
1055 35. Koehler, M., Petitjean, S.J.L., Yang, J., Aravamudhan, P., Somoulay, X., Lo
1056 Giudice, C., Poncin, M.A., Dumitru, A.C., Dermody, T.S., and Alsteens, D.
1057 (2021). Reovirus directly engages integrin to recruit clathrin for entry into host
1058 cells. Nat Commun *12*, 2149. 10.1038/s41467-021-22380-0.
1059 36. Ortega-González, P., Taylor, G., Jangra, R.K., Tenorio, R., Fernández de Castro,
1060 I., Mainou, B.A., Orchard, R.C., Wilen, C.B., Brigleb, P.H., Sojati, J., et al. (2022).
1061 Reovirus infection is regulated by NPC1 and endosomal cholesterol
1062 homeostasis. PLoS Pathog *18*, e1010322. 10.1371/journal.ppat.1010322.
1063 37. Barrass, S.V., and Butcher, S.J. (2020). Advances in high-throughput methods
1064 for the identification of virus receptors. Med Microbiol Immunol *209*, 309-323.
1065 10.1007/s00430-019-00653-2.
1066 38. Puschnik, A.S., Majzoub, K., Ooi, Y.S., and Carette, J.E. (2017). A CRISPR
1067 toolbox to study virus-host interactions. Nat Rev Microbiol *15*, 351-364.
1068 10.1038/nrmicro.2017.29.
1069 39. Dermody, T.S., Nibert, M.L., Bassel-Duby, R., and Fields, B.N. (1990). A s1
1070 region important for hemagglutination by serotype 3 reovirus strains. J Virol *64*,
1071 5173-5176.

1072 40. Alsteens, D., Newton, R., Schubert, R., Martinez-Martin, D., Delguste, M., Roska,
1073 B., and Müller, D.J. (2017). Nanomechanical mapping of first binding steps of a
1074 virus to animal cells. Nat Nanotechnol *12*, 177-183. 10.1038/nnano.2016.228.
1075 41. Diller, J.R., Halloran, S.R., Koehler, M., dos Santos Natividade, R., Alsteens, D.,
1076 Stehle, T., Dermody, T.S., and Ogden, K.M. (2020). Reovirus σ1 conformational
1077 flexibility modulates the efficiency of host cell attachment. J Virol *94*, e01163-
1078 01120. 10.1128/jvi.01163-20.
1079 42. dos Santos Natividade, R., Koehler, M., Gomes, P., Simpson, J.D., Smith, S.C.,
1080 Gomes, D.E.B., de Lhoneux, J., Yang, J., Ray, A., Dermody, T.S., et al. (2023).
1081 Deciphering molecular mechanisms stabilizing the reovirus-binding complex.
1082 Proc Natl Acad Sci U S A *120*, e2220741120. 10.1073/pnas.2220741120.
1083 43. Sutherland, D.M., Strebl, M., Koehler, M., Welsh, O.L., Yu, X., Hu, L., dos Santos
1084 Natividade, R., Knowlton, J.J., Taylor, G.M., Moreno, R.A., et al. (2023). NgR1
1085 binding to reovirus reveals an unusual bivalent interaction and a new viral
1086 attachment protein. Proc Natl Acad Sci U S A *120*, e2219404120.
1087 10.1073/pnas.2219404120.
1088 44. Evans, E., and Ritchie, K. (1997). Dynamic strength of molecular adhesion
1089 bonds. Biophys J *72*, 1541-1555. 10.1016/s0006-3495(97)78802-7.
1090 45. Evans, E.A., and Calderwood, D.A. (2007). Forces and bond dynamics in cell
1091 adhesion. Science *316*, 1148-1153. 10.1126/science.1137592.
1092 46. Rankl, C., Kienberger, F., Wildling, L., Wruss, J., Gruber, H.J., Blaas, D., and
1093 Hinterdorfer, P. (2008). Multiple receptors involved in human rhinovirus

1094 attachment to live cells. Proc Natl Acad Sci U S A *105*, 17778-17783.
1095 10.1073/pnas.0806451105.
1096 47. Appleton, B.A., Wu, P., Maloney, J., Yin, J., Liang, W.C., Stawicki, S., Mortara,
1097 K., Bowman, K.K., Elliott, J.M., Desmarais, W., et al. (2007). Structural studies of
1098 neuropilin/antibody complexes provide insights into semaphorin and VEGF
1099 binding. Embo j *26*, 4902-4912. 10.1038/sj.emboj.7601906.
1100 48. Janssen, B.J., Malinauskas, T., Weir, G.A., Cader, M.Z., Siebold, C., and Jones,
1101 E.Y. (2012). Neuropilins lock secreted semaphorins onto plexins in a ternary
1102 signaling complex. Nat Struct Mol Biol *19*, 1293-1299. 10.1038/nsmb.2416.
1103 49. Reinisch, K.M., Nibert, M., and Harrison, S.C. (2000). Structure of the reovirus
1104 core at 3.6 angstrom resolution. Nature *404*, 960-967.
1105 50. Liemann, S., Chandran, K., Baker, T.S., Nibert, M.L., and Harrison, S.C. (2002).
1106 Structure of the reovirus membrane-penetration protein, μ1, in a complex with its
1107 protector protein, σ3. Cell *108*, 283-295.
1108 51. Zhang, X., Ji, Y., Zhang, L., Harrison, S.C., Marinescu, D.C., Nibert, M.L., and
1109 Baker, T.S. (2005). Features of reovirus outer capsid protein μ1 revealed by
1110 electron cryomicroscopy and image reconstruction of the virion at 7.0 Å
1111 resolution. Structure *13*, 1545-1557. 10.1016/j.str.2005.07.012.
1112 52. Maginnis, M.S., Forrest, J.C., Kopecky-Bromberg, S.A., Dickeson, S.K., Santoro,
1113 S.A., Zutter, M.M., Nemerow, G.R., Bergelson, J.M., and Dermody, T.S. (2006).
1114 β1 integrin mediates internalization of mammalian reovirus. J Virol *80*, 2760-
1115 2770.

1116 53. Koyuncu, O.O., Hogue, I.B., and Enquist, L.W. (2013). Virus infections in the
1117 nervous system. Cell Host Microbe *13*, 379-393. 10.1016/j.chom.2013.03.010.
1118 54. Ayala-Nunez, N.V., and Gaudin, R. (2020). A viral journey to the brain: current
1119 considerations and future developments. PLoS Pathog *16*, e1008434.
1120 10.1371/journal.ppat.1008434.
1121 55. Chappell, J.D., Barton, E.S., Smith, T.H., Baer, G.S., Duong, D.T., Nibert, M.L.,
1122 and Dermody, T.S. (1998). Cleavage susceptibility of reovirus attachment protein
1123 σ1 during proteolytic disassembly of virions is determined by a sequence
1124 polymorphism in the σ1 neck. J Virol *72*, 8205-8213.
1125 56. Nibert, M.L., Chappell, J.D., and Dermody, T.S. (1995). Infectious subvirion
1126 particles of reovirus type 3 Dearing exhibit a loss in infectivity and contain a
1127 cleaved σ1 protein. J Virol *69*, 5057-5067. 10.1128/jvi.69.8.5057-5067.1995.
1128 57. Kong, W., Montano, M., Corley, M.J., Helmy, E., Kobayashi, H., Kinisu, M.,
1129 Suryawanshi, R., Luo, X., Royer, L.A., Roan, N.R., et al. (2022). Neuropilin-1
1130 mediates SARS-CoV-2 infection of astrocytes in brain organoids, inducing
1131 inflammation leading to dysfunction and death of neurons. mBio *13*, e0230822.
1132 10.1128/mbio.02308-22.
1133 58. Joyce, J.D., Moore, G.A., Goswami, P., Harrell, T.L., Taylor, T.M., Hawks, S.A.,
1134 Green, J.C., Jia, M., Yallayi, N., Leslie, E.H., et al. (2023). SARS-CoV-2 infects
1135 peripheral and central neurons before viremia, facilitated by neuropilin-1. bioRxiv.
1136 10.1101/2022.05.20.492834.
1137 59. Sutherland, D.M., Aravamudhan, P., Dietrich, M.H., Stehle, T., and Dermody,
1138 T.S. (2018). Reovirus neurotropism and virulence are dictated by sequences in

1139 the head domain of the viral attachment protein. J Virol *92*, e00974-00918.
1140 10.1128/JVI.00974-18.
1141 60. Pan, M., Alvarez-Cabrera, A.L., Kang, J.S., Wang, L., Fan, C., and Zhou, Z.H.
1142 (2021). Asymmetric reconstruction of mammalian reovirus reveals interactions
1143 among RNA, transcriptional factor μ2 and capsid proteins. Nat Commun *12*,
1144 4176. 10.1038/s41467-021-24455-4.
1145 61. Bao, K., Zhang, X., Li, D., Sun, W., Sun, Z., Wang, J., and Zhu, P. (2022). In situ
1146 structures of polymerase complex of mammalian reovirus illuminate RdRp
1147 activation and transcription regulation. Proc Natl Acad Sci U S A *119*,
1148 e2203054119. 10.1073/pnas.2203054119.
1149 62. Excoffon, K.J.D.A., Guglielmi, K.M., Wetzel, J.D., Gansemer, N.D., Campbell,
1150 J.A., Dermody, T.S., and Zabner, J. (2008). Reovirus preferentially infects the
1151 basolateral surface and is released from the apical surface of polarized human
1152 respiratory epithelial cells. J Infect Dis *197*, 1189-1197. 10.1086/529515.
1153 63. Lai, C.M., Mainou, B.A., Kim, K.S., and Dermody, T.S. (2013). Directional release
1154 of reovirus from the apical surface of polarized endothelial cells. mBio *4*, e00049-
1155 00013. 10.1128/mBio.00049-13.
1156 64. Li, J., Liu, T., Dong, Y., Kondoh, K., and Lu, Z. (2019). Trans-synaptic neural
1157 circuit-tracing with neurotropic viruses. Neuroscience bulletin *35*, 909-920.
1158 65. Zhang, J., Yang, H., Wu, J., Zhang, D., Wang, Y., and Zhai, J. (2022). Recent
1159 progresses in novel in vitro models of primary neurons: a biomaterial perspective.
1160 Front Bioeng Biotechnol *10*, 953031. 10.3389/fbioe.2022.953031.

1161 66. Fraser, R.D., Furlong, D.B., Trus, B.L., Nibert, M.L., Fields, B.N., and Steven,
1162 A.C. (1990). Molecular structure of the cell-attachment protein of reovirus:
1163 correlation of computer-processed electron micrographs with sequence-based
1164 predictions. J Virol *64*, 2990-3000.
1165 67. Li, Z.L., and Buck, M. (2021). Neuropilin-1 assists SARS-CoV-2 infection by
1166 stimulating the separation of spike protein S1 and S2. Biophys J *120*, 2828-2837.
1167 10.1016/j.bpj.2021.05.026.
1168 68. Dietrich, M.H., Ogden, K.M., Long, J.M., Ebenhoch, R., Thor, A., Dermody, T.S.,
1169 and Stehle, T. (2018). Structural and functional features of the reovirus σ1 tail. J
1170 Virol *92*, e00336-00318. 10.1128/JVI.00336-18.
1171 69. Larson, S.M., Antczak, J.B., and Joklik, W.K. (1994). Reovirus exists in the form
1172 of 13 particle species that differ in their content of protein sigma-1. Virology *201*,
1173 303-311. DOI 10.1006/viro.1994.1295.
1174 70. Sironi, M., Cagliani, R., Forni, D., and Clerici, M. (2015). Evolutionary insights
1175 into host-pathogen interactions from mammalian sequence data. Nat Rev Genet
1176 *16*, 224-236. 10.1038/nrg3905.
1177 71. Sanson, K.R., Hanna, R.E., Hegde, M., Donovan, K.F., Strand, C., Sullender,
1178 M.E., Vaimberg, E.W., Goodale, A., Root, D.E., Piccioni, F., and Doench, J.G.
1179 (2018). Optimized libraries for CRISPR-Cas9 genetic screens with multiple
1180 modalities. Nat Commun *9*, 5416. 10.1038/s41467-018-07901-8.
1181 72. Aravamudhan, P., Raghunathan, K., Konopka-Anstadt, J., Pathak, A.,
1182 Sutherland, D.M., Carter, B.D., and Dermody, T.S. (2020). Reovirus uses

1183 macropinocytosis-mediated entry and fast axonal transport to infect neurons.
1184 PLoS Pathog *16*, e1008380. 10.1371/journal.ppat.1008380.
1185 73. Kobayashi, T., Ooms, L.S., Ikizler, M., Chappell, J.D., and Dermody, T.S. (2010).
1186 An improved reverse genetics system for mammalian orthoreoviruses. Virology
1187 *398*, 194-200. 10.1016/j.virol.2009.11.037.
1188 74. Wildling, L., Unterauer, B., Zhu, R., Rupprecht, A., Haselgrübler, T., Rankl, C.,
1189 Ebner, A., Vater, D., Pollheimer, P., Pohl, E.E., et al. (2011). Linking of sensor
1190 molecules with amino groups to amino-functionalized AFM tips. Bioconjug Chem
1191 *22*, 1239-1248. 10.1021/bc200099t.
1192 75. Ebner, A., Hinterdorfer, P., and Gruber, H.J. (2007). Comparison of different
1193 aminofunctionalization strategies for attachment of single antibodies to AFM
1194 cantilevers. Ultramicroscopy *107*, 922-927. 10.1016/j.ultramic.2007.02.035.
1195 76. Dupres, V., Menozzi, F.D., Locht, C., Clare, B.H., Abbott, N.L., Cuenot, S.,
1196 Bompard, C., Raze, D., and Dufrêne, Y.F. (2005). Nanoscale mapping and
1197 functional analysis of individual adhesins on living bacteria. Nature methods *2*,
1198 515-520.
1199 77. Butt, H.-J., and Jaschke, M. (1995). Calculation of thermal noise in atomic force
1200 microscopy. Nanotechnology *6*, 1.
1201 78. Bustamante, C., Marko, J.F., Siggia, E.D., and Smith, S. (1994). Entropic
1202 elasticity of λ-phage DNA. Science *265*, 1599-1600.
1203 79. Newton, R., Delguste, M., Koehler, M., Dumitru, A.C., Laskowski, P.R., Müller,
1204 D.J., and Alsteens, D. (2017). Combining confocal and atomic force microscopy

1205 to quantify single-virus binding to mammalian cell surfaces. Nature protocols *12*,
1206 2275-2292.
1207 80. Alsteens, D., Newton, R., Schubert, R., Martinez-Martin, D., Delguste, M., Roska,
1208 B., and Müller, D.J. (2017). Nanomechanical mapping of first binding steps of a
1209 virus to animal cells. Nature nanotechnology *12*, 177-183.
1210 81. Rankl, C., Wildling, L., Neundlinger, I., Kienberger, F., Gruber, H., Blaas, D., and
1211 Hinterdorfer, P. (2011). Determination of the kinetic on-and off-rate of single
1212 virus–cell interactions. Atomic Force Microscopy in Biomedical Research:
1213 Methods and Protocols, 197-210.
1214 82. Evans, E.A., and Calderwood, D.A. (2007). Forces and bond dynamics in cell
1215 adhesion. Science *316*, 1148-1153.
1216 83. Williams, P.M. (2003). Analytical descriptions of dynamic force spectroscopy:
1217 behaviour of multiple connections. Analytica Chimica Acta *479*, 107-115.

1218

Figure 1. mNRP1 promotes reovirus binding and infection

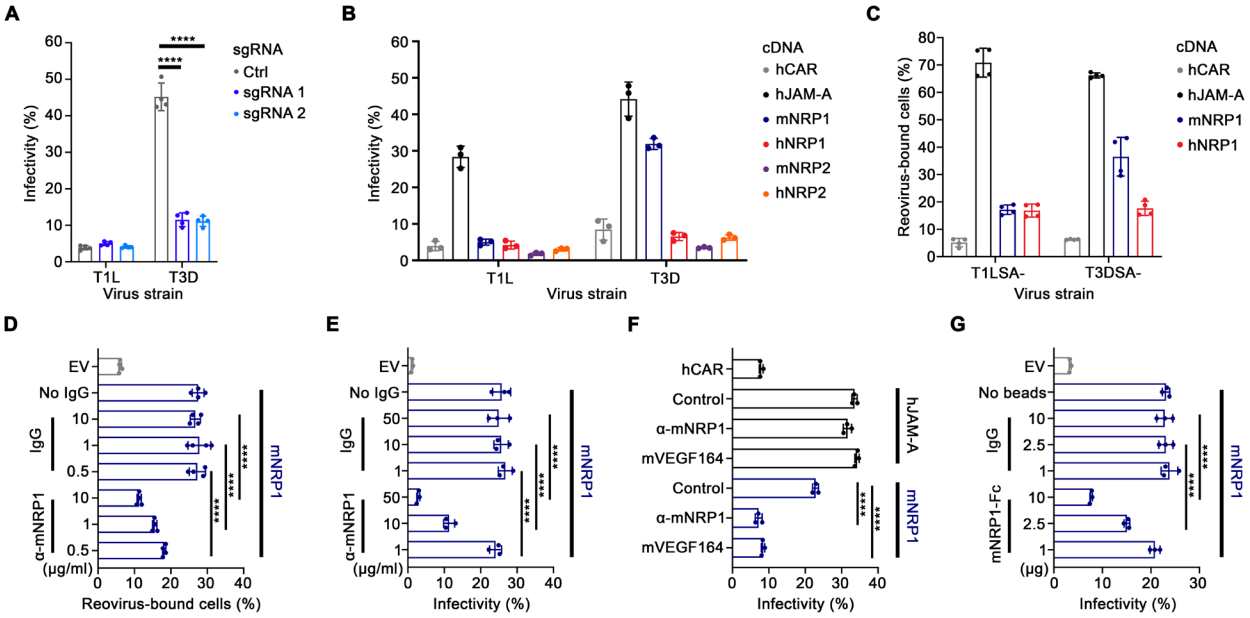

Figure 2. Biophysics of reovirus-NRP1 interactions

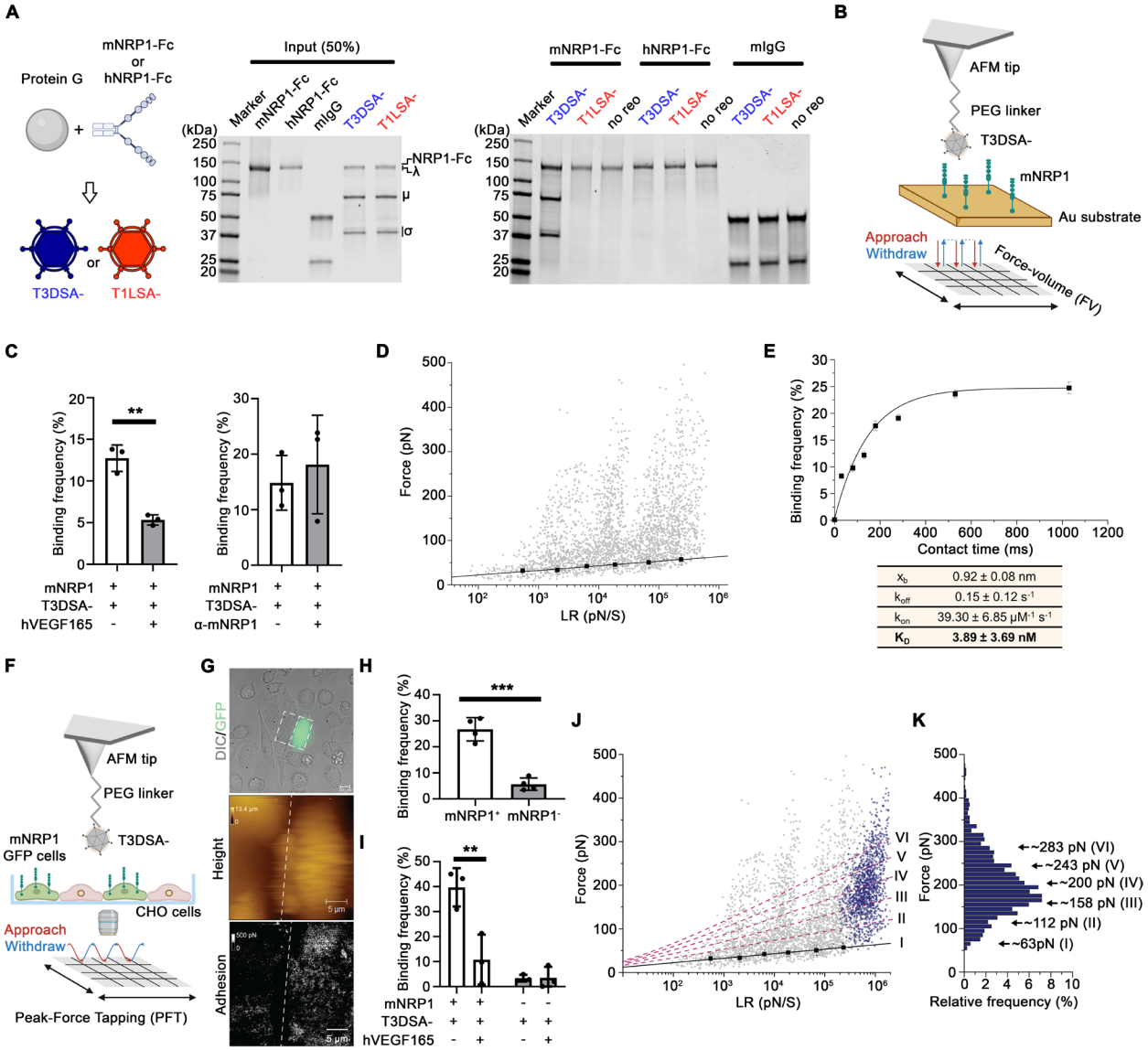

Figure 3. Reovirus-NRP1 interactions require multiple NRP1 extracellular domains

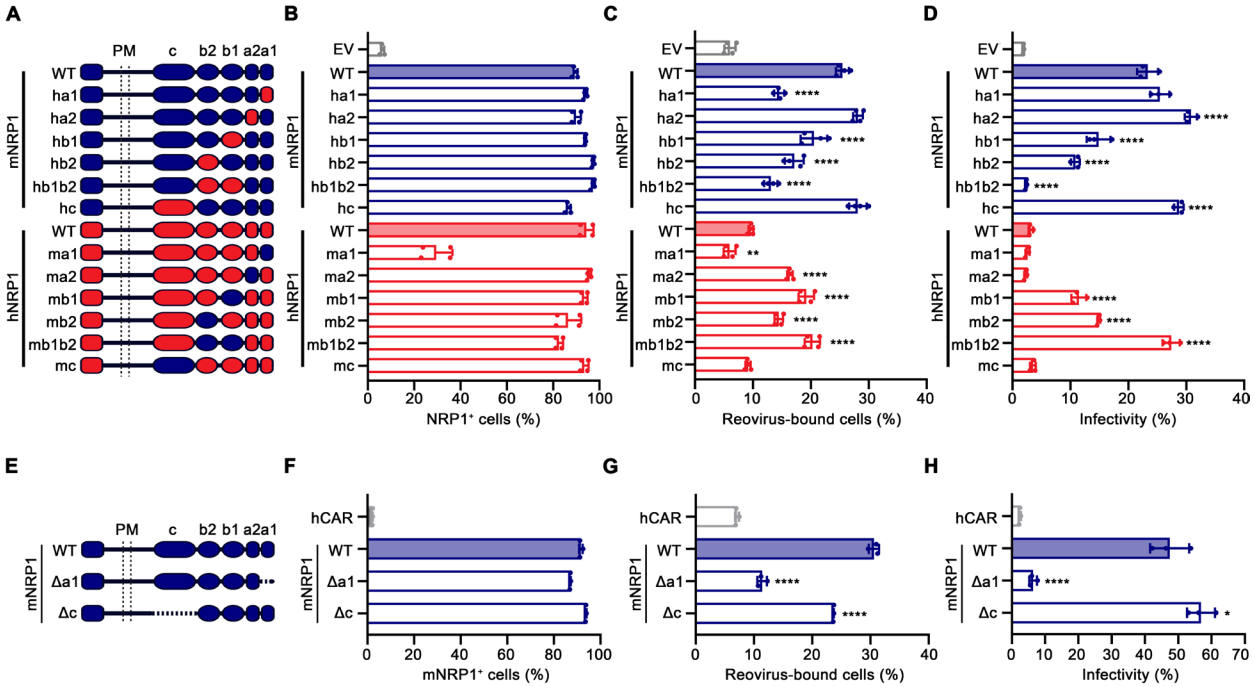

Figure 4. Multiple reovirus capsid proteins are required for interactions with NRP1

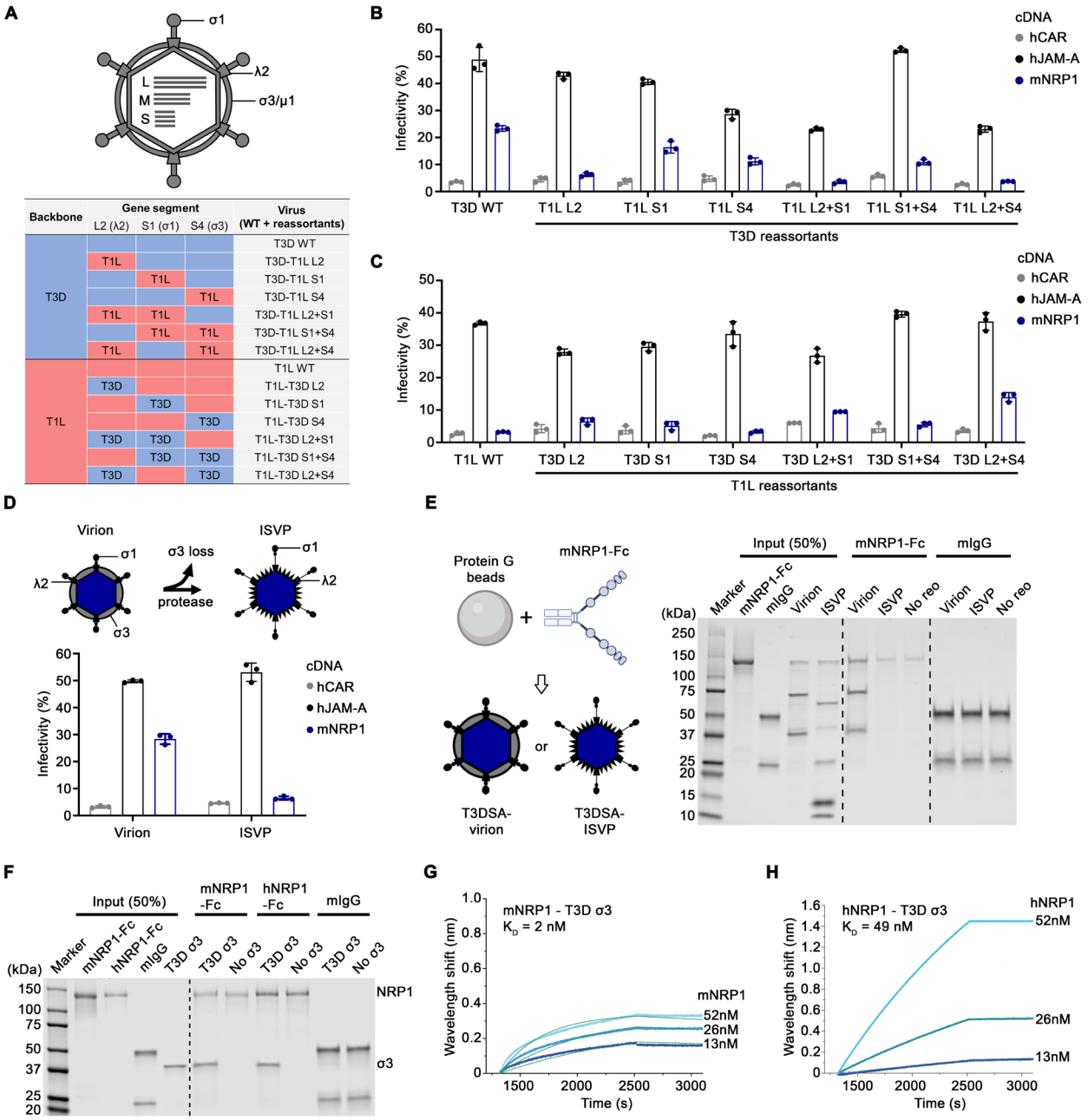

Backbone	Gene segment L2 (λ2)	S1 (σ1)	S4 (σ3)	Virus (WT + reassortants)
T3D				T3D WT
	T1L			T3D-T1L L2
		T1L		T3D-T1L S1
			T1L	T3D-T1L S4
	T1L	T1L		T3D-T1L L2+S1
		T1L	T1L	T3D-T1L S1+S4
	T1L		T1L	T3D-T1L L2+S4
T1L				T1L WT
	T3D			T1L-T3D L2
		T3D		T1L-T3D S1
			T3D	T1L-T3D S4
	T3D	T3D		T1L-T3D L2+S1
		T3D	T3D	T1L-T3D S1+S4
	T3D		T3D	T1L-T3D L2+S4

Figure 5. Capsid turret protein λ2 contributes to NRP1 binding and is required for NRP1-mediated infectivity

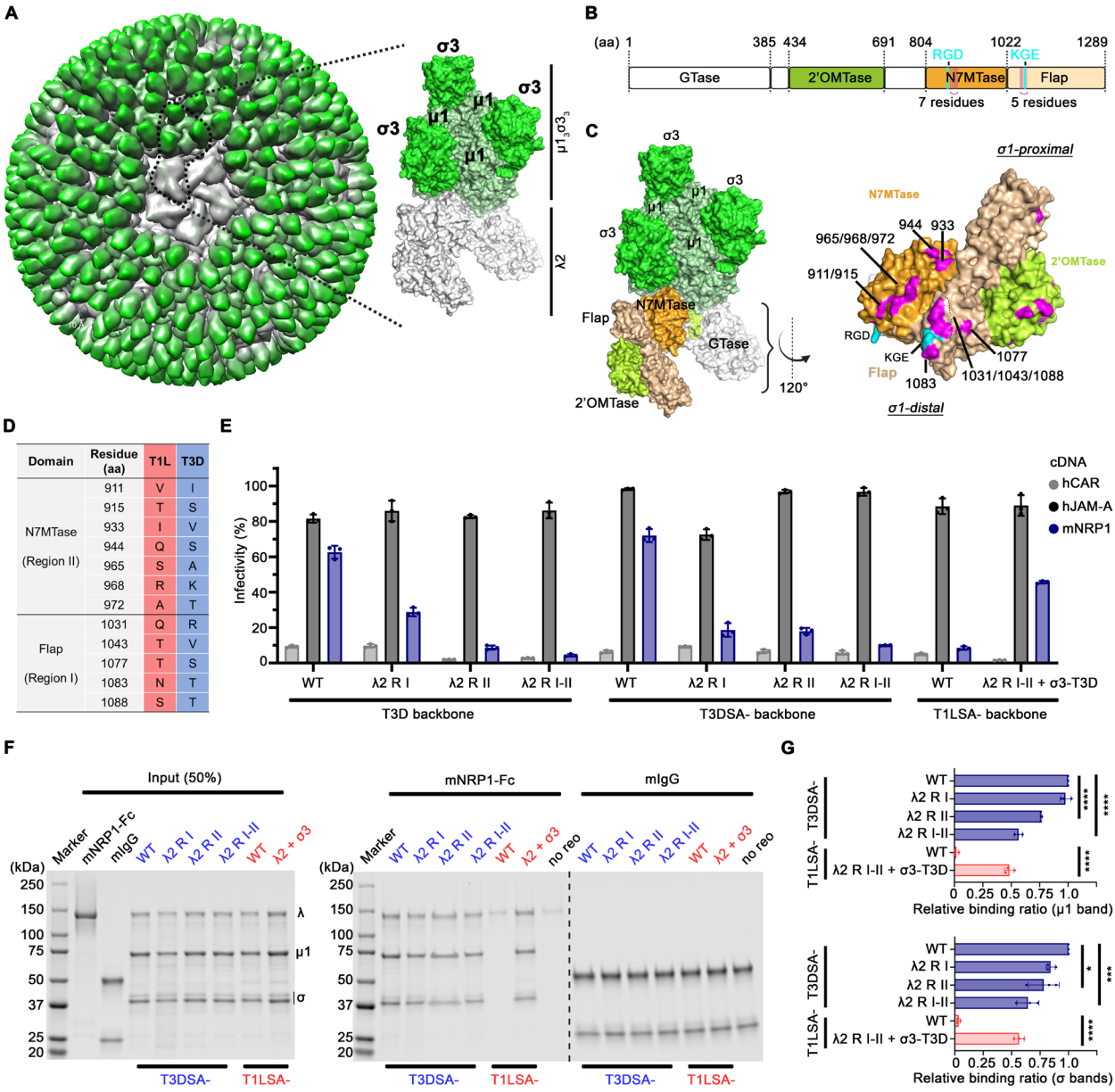

Domain	Residue (aa)	T1L	T3D
N7MTase (Region II)	911	V	I
	915	T	S
	933	I	V
	944	Q	S
	965	S	A
	968	R	K
	972	A	T
Flap (Region I)	1031	Q	R
	1043	T	V
	1077	T	S
	1083	N	T
	1088	S	T

Figure 6. Protomers of outer-capsid protein σ3 are engaged in interactions with NRP1

A

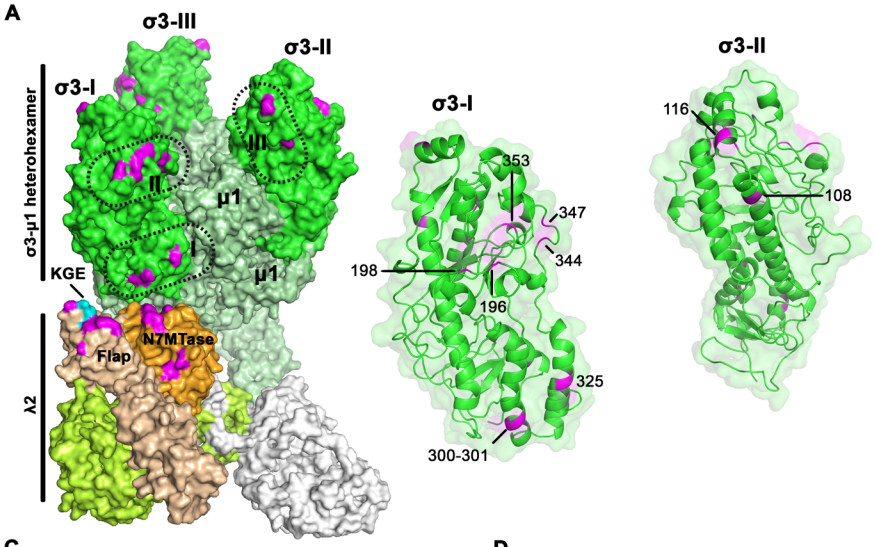

B

Domain	Residue (aa)	T1L	T3D
Patch I	300	D	E
	301	S	A
	325	D	N
Patch II	196	R	K
	198	E	G
	344	S	P
	347	T	I
	353	D	N
Patch III	108	A	E
	116	E	D

C

T3DSA- mutant	σ3 mutations	λ2 mutations
σ3 P I	Patch I	WT
σ3 P I-II	Patch I + II	WT
σ3 P I-III	Patch I + III	WT
σ3-T1L	T1L σ3	WT
σ3 P I + λ2 R I-II	Patch I	Flap + N7MTase
σ3 P I-II + λ2 R I-II	Patch I + II	Flap + N7MTase
σ3 P I-III + λ2 R I-II	Patch I + III	Flap + N7MTase
σ3-T1L + λ2 R I-II	T1L σ3	Flap + N7MTase

D

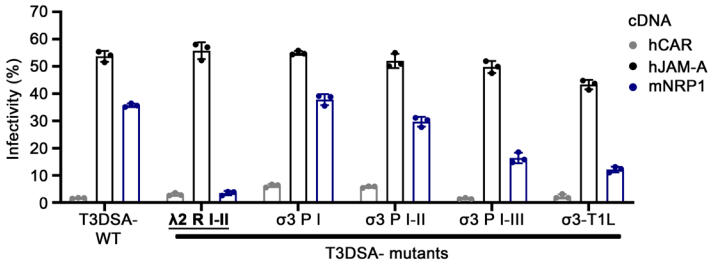

E

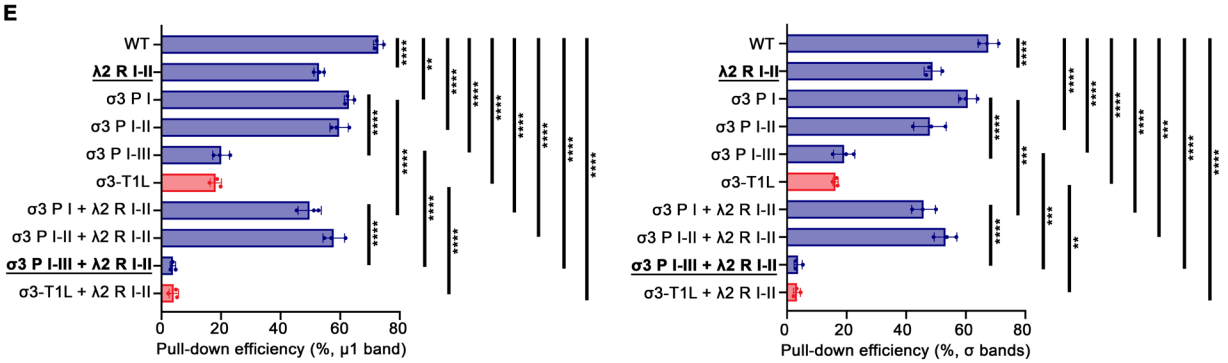

F

Backbone	Mutant	Mutations	
		σ3	λ2
T3DSA-	σ3 P III	Patch III	WT
	σ3 P III + λ2 R I-II	Patch III	Flap + N7MTase
T1LSA-	σ3 P III	Patch III	WT
	σ3 P III + λ2 R I-II	Patch III	Flap + N7MTase

G

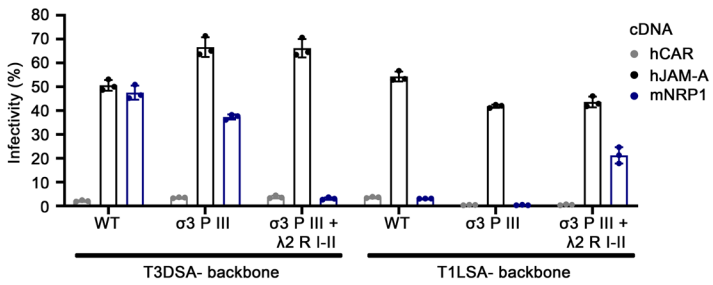

H

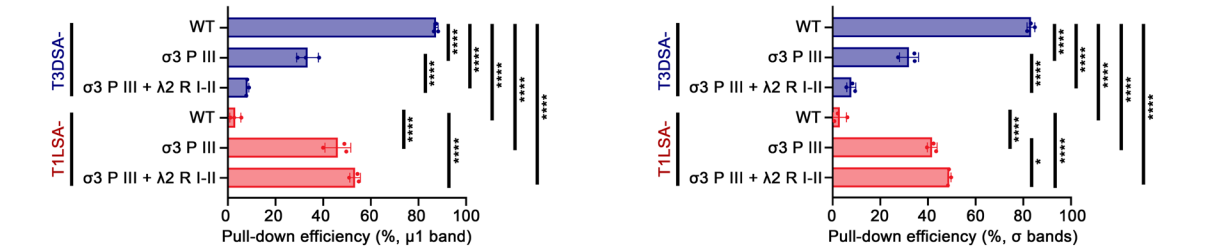

Figure 7. NRP1 contributes to reovirus dissemination and neurovirulence in mice